

COMPARISON OF SOLID ROCKET MOTOR THRUST MODULATION TECHNIQUES

by

Clayton Edward Wozney

Bachelor of Engineering, Ryerson University (2013)

Bachelor of Science, Brandon University (1987)

A thesis

presented to Ryerson University

in partial fulfillment of the

requirements for the degree of

Master of Applied Science

in the program of

Aerospace Engineering

Toronto, Ontario, Canada, 2017

© Clayton Wozney 2017

AUTHOR'S DECLARATION FOR ELECTRONIC SUBMISSION OF A THESIS

I hereby declare that I am the sole author of this thesis. This is a true copy of the thesis, including any required final revisions, as accepted by my examiners.

I authorize Ryerson University to lend this thesis to other institutions or individuals for the purpose of scholarly research.

I further authorize Ryerson University to reproduce this thesis by photocopying or by other means, in total or in part, at the request of other institutions or individuals for the purpose of scholarly research.

I understand that my thesis may be made electronically available to the public.

COMPARISON OF SOLID ROCKET MOTOR THRUST MODULATION TECHNIQUES

Clayton Wozney, Aerospace Engineering, MAsc, Ryerson University, 2017

Abstract

The thrust profiles of solid rocket motors are usually determined ahead of time by propellant composition and grain design. Traditional techniques for active thrust modulation use a moveable pintle to dynamically change the nozzle throat diameter, increasing the chamber pressure and therefore thrust. With this approach, high chamber pressures must be endured with only modest increases in thrust. Alternatively, it has been shown that spinning a solid rocket motor on its longitudinal axis can increase the burning rate of the propellant and therefore the thrust without the resulting high chamber pressures. Building on prior experience modelling pressure-dependent, flow-dependent and acceleration-dependent burning in solid rocket motors, an internal ballistic simulation computer program is modified for the present study where the use of the pintle nozzle and spin-augmented solid rocket motor combustion approaches, for a reference cylindrical-grain motor, are compared. This study confirms that comparable thrust augmentation can be gained at lower chamber pressures using the novel spin-acceleration approach, relative to the established pintle-nozzle approach, thus potentially providing a significant design advantage.

Acknowledgements

I would like to thank Dr. David Greatrix for all of his patience and guidance during the research and writing of this thesis, and Mr. Jerry Karpynczyk and Mr. Peter Bradley for their moral support and constant enthusiasm for the project.

Dedication

I dedicate this master's thesis to my wonderful and ever-supportive wife Deidra, whose constant encouragement and personal sacrifice allowed me to complete this endeavour.

Table of Contents

Abstract	iii
Acknowledgements	iv
Dedication	v
List of Tables	ix
List of Figures	x
Nomenclature	xii
1 Introduction	1
2 Solid Propellant Burning Rate Models	7
2.1 Pressure Dependent Burning	9
2.2 Erosive Burning	10
2.3 Acceleration Effects on Burning Rate	13
3 Thrust Modulation of Solid Rocket Motors	20
3.1 Burning Rate Augmentation Due to Increased Chamber Pressure	20

3.2	Burning Rate Augmentation Due to Normal Acceleration	22
3.3	Acceleration Effects in Metallized and Non-Metallized Propellants	23
3.4	Effects of Orientation Angle on Acceleration Effects	24
4	Internal Ballistic Modelling and Analysis	26
4.1	Equations of Motion	26
4.1.1	Gas Phase	26
4.1.2	Particle Phase	27
4.2	Computer Modelling of Internal Ballistics	28
4.3	Reference Motor	28
5	Simulation Results	31
5.1	Reference Motor	31
5.2	Pintle Nozzle Motor	34
5.3	Spinning Rocket Motor	36
5.4	Comparison of Pintle Nozzle and Spinning SRM	37
5.5	Spinning Rocket at Maximum Chamber Pressure	40
5.6	Spinning Rocket With Longitudinal Acceleration	43
6	Discussion of Results	48
6.1	Implementation Strategies for a Spinning SRM	50

7 Conclusion	55
8 Considerations for Future Work	57
References	58

List of Tables

1.1	Characteristics of various solid propellants	2
4.1	Summary of the reference solid rocket motor simulation parameters .	30
5.1	Summary of the simulation results	44

List of Figures

1.1	Structural features found on solid rocket motors	3
1.2	Thrust profiles from various grain geometries	4
1.3	Cutaway diagram of a finocyl propellant grain in an SRM	5
2.1	Pressure-dependant burning rate behaviour	10
2.2	Schematic diagram of combustion zone stretching	12
2.3	Theoretical and experimental data for burning rate augmentation . . .	13
2.4	Burning rate augmentation as a function of normal acceleration . . .	15
2.5	Burning rate augmentation as a function of resultant acceleration angle	16
2.6	Head-end pressure-time profiles of solid rocket motor, baseline	17
2.7	Head-end pressure-time profiles of solid rocket motor, 15g	18
2.8	Sea-level thrust-time profiles of solid rocket motor, 15g	19
3.1	Moveable pintle varying the throat area of the nozzle	21
3.2	SRM spinning as a means of inducing a normal acceleration field . . .	23
3.3	Schematic diagram of acceleration vectors acting near the propellant surface	23
5.1	Chamber pressure-time profile for reference motor firing	32
5.2	Sea-level thrust-time profile for reference motor firing	33

5.3	Chamber pressure-time profile for pintle motor firing	34
5.4	Thrust-time profile for pintle motor firing	35
5.5	Chamber pressure-time profile for spinning motor firing, 10 rps	36
5.6	Sea-level thrust-time profile for spinning motor firing, 10 rps	37
5.7	Chamber pressure-time profiles for all motor firings	38
5.8	Sea-level thrust-time profiles for all motor firings	39
5.9	Sea-level chamber pressure-time profile for spinning rocket motor firing, 18 rps	41
5.10	Sea-level thrust-time profile for spinning rocket motor firing, 18 rps	42
5.11	Sea-level chamber pressure-time profile for spinning rocket motor firing with lateral acceleration	44
5.12	Sea-level thrust-time profile for spinning rocket motor firing with longitudinal acceleration	45
5.13	Sea-level chamber pressure-time profile for boosted spin rate	46
5.14	Sea-level thrust-time profile for boosted spin rate	47
6.1	Variable incident tail fins for inducing spin	51
6.2	Cutaway of spinning rocket with SRM rotated independently of the airframe	52
6.3	Cutaway of externally spun SRM rotated independently of the airframe on the launch pad	53
6.4	Schematic of an externally spun rocket airframe	54

Nomenclature

Symbols

A_e	Nozzle exit plane cross-sectional area, m^2
A_t	Nozzle throat cross-sectional area, m^2
a_l	Longitudinal (or lateral) acceleration, m s^{-2}
a_n	Normal acceleration, m s^{-2}
C	de St. Robert's law coefficient, $\text{m s}^{-1} \text{Pa}^{-n}$
C_F	Thrust coefficient [rocket engine]
C_o	de St. Robert's law coefficient, reference conditions, $\text{m s}^{-1} \text{Pa}^{-n}$
C_p	Constant-pressure specific heat, gas phase, $\text{J kg}^{-1} \text{K}^{-1}$
C_s	Specific heat, solid phase, $\text{J kg}^{-1} \text{K}^{-1}$
$C_{F,v}$	Vacuum thrust coefficient
D	Aerodynamic drag, N
d_m	Particle mean diameter m
d_p	Port diameter, m
f	Darcy-Weisbach friction factor
f^*	Zero-transpiration friction factor
f_{lim}	Limit friction factor for negative erosive burning
G	Axial mass flux, $\text{kg m}^{-2} \text{s}^{-1}$
G_a	Accelerative mass flux, $\text{kg m}^{-2} \text{s}^{-1}$

ΔH_s	Net surface heat release, J kg^{-1}
h	Effective convective heat transfer coefficient, $\text{W m}^{-2} \text{K}^{-1}$
h^*	Zero-transpiration convective heat transfer coefficient, $\text{W m}^{-2} \text{K}^{-1}$
K	Lateral/longitudinal acceleration burning rate displacement orientation angle coefficient
K_δ	Shear layer coefficient, m^{-1}
k	Gas thermal conductivity, $\text{W m}^{-1} \text{K}^{-1}$
M	Atomic mass unit, amu
\dot{m}_e	Mass flow through the nozzle exit, kg s^{-1}
\dot{m}_t	Mass flow through the nozzle throat, kg s^{-1}
n	Pressure-dependent burning rate exponent
p_e	Nozzle exit static pressure, Pa
p_∞	Outside ambient air pressure, Pa
Q	Heat transfer rate, W
R	Specific gas constant, $\text{J kg}^{-1} \text{K}^{-1}$
Re_d	Local gas Reynold's number based on core hydraulic diameter
r_b	Overall burning rate, m s^{-1}
r_e	Erosive burning rate positive component, m s^{-1}
r_o	Base burning rate, m s^{-1}
r_p	Pressure-dependent burning rate, m s^{-1}
S_p	Propellant surface area, m^2
T_f	Flame temperature, K
T_i	Initial temperature, solid phase, K

T_s	Burning surface temperature, K
T_{io}	Initial temperature, solid phase, reference conditions, K
u_e	Nozzle exit gas or exhaust jet velocity, m s^{-1}
u_{eff}	Effective gas velocity parallel to propellant surface, m s^{-1}
u_∞	Bulk axial gas velocity, m s^{-1}
v_f	Normal gas flow velocity of flame, m s^{-1}
α_p	Particle mass loading fraction
δ_o	Reference energy zone thickness, m
δ_r	Resultant energy zone thickness, m
ϵ	Effective propellant surface roughness height, m
γ	Ratio of specific heats of gas
μ	Absolute [dynamic] gas viscosity, $\text{kg m}^{-1} \text{s}^{-1}$
ϕ	Acceleration vector angle, $^\circ$
ϕ_d	Acceleration vector displacement orientation angle, $^\circ$
ρ	Local gas density, kg m^{-3}
ρ_p	Density, particles within gas flow volume, kg m^{-3}
ρ_s	Density, solid phase, kg m^{-3}
σ_p	Pressure-dependant burning rate temperature sensitivity, K^{-1}
Θ_r	Resultant angle of stretched energy zone, $^\circ$

Acronyms

AP	Ammonium perchlorate, (crystalline oxidizer)
CTPB	Carboxy-terminated polybutadiene (solid fuel)
EPON	Epoxy resin

MN	Mega-Newton
NC	Nitrocellulose, (solid monopropellant)
NG	Nitroglycerine, (liquid monopropellant/explosive; solid when combined with NC)
PBAA	Polybutadiene acrylic acid (solid fuel)
PBAN	Polybutadiene-acrylic acid-acrylonitrile terpolymer (solid fuel)
PS	Polysulfide
PU	Polyurethane
QUROC	QUasi-steady ROCKET (code)
SRM	Solid propellant rocket motor

1 Introduction

A solid propellant rocket motor (SRM) is nominally one of the simpler chemical rocket propulsion systems. Often with no moving parts, SRMs can be very straightforward to operate; that is, once ignited, the SRM burns to completion based on its physical and chemical characteristics as defined at the time of design and manufacture without any dynamic throttle or thrust control. SRMs range in thrust delivery from μN thrusters on mini-satellites to MN class boosters for space launch vehicles [1]. For single burn applications, they are often the most cost-effective propulsion system among various alternatives (e.g., liquid or hybrid rocket engines).

The nominal performance of solid rocket motors is determined primarily by their propellant constituents, formulation and grain geometry. The propellant formulations of SRMs typically consist of a fuel, oxidizer, binder, and optionally various small quantities of combustion modifiers. Table 1.1 [1] shows some common combinations of fuel and oxidizers used in operational SRMs. A typical SRM consists of one or more propellant grains, cast or assembled into a thin casing capable of withstanding the intended combustion pressures, closed at one end with a divergent or convergent-divergent nozzle at the other end as shown in Fig. 1.1 [2]¹.

To prevent the casing material from being exposed to the high combustion tem-

¹The thrust termination opening device shown is something often used on large SRMs which allows the thrust of the SRM to be immediately cut off by essentially blowing the front end of the SRM off. This gives the flight control system a one-shot ability to dynamically (and dramatically) control the thrust profile and firing time to more accurately place a payload or munition.

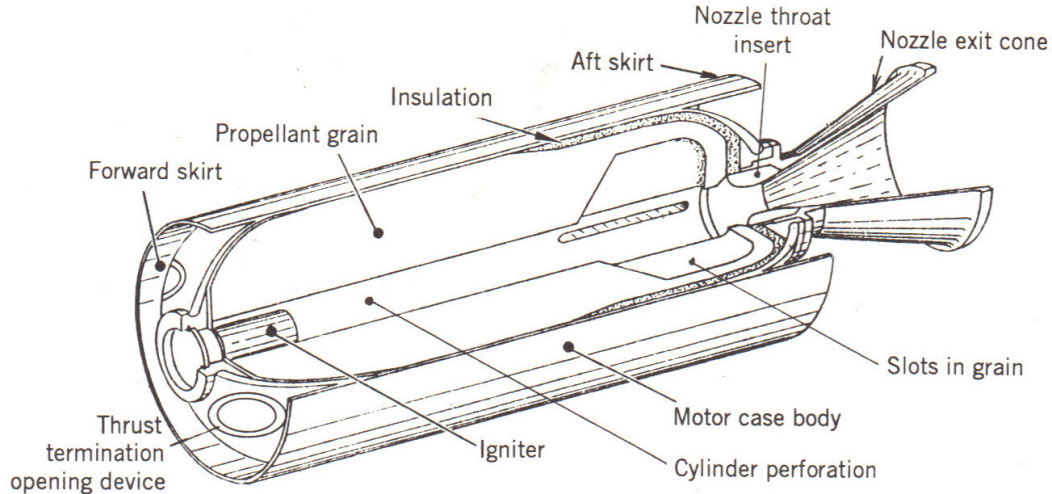
Table 1.1: Characteristics of various solid propellants at nominal operating conditions^b

Propellant ^a	ρ_s (kg m ⁻³)	T_f (K)	T_S (K)	M (amu)	γ	r_b (m s ⁻¹)
NC/NG	1630	2300	760	22	1.26	0.007
AP/PS/additives	1635	2500	780	25	1.23	0.008
AP/PU/additives	1620	2400	670	21	1.25	0.005
AP/PBAA/EPON	1600	2300	700	22	1.24	0.008
AP/PBAN/Al	1750	2600	800	24	1.24	0.010
AP/CTPB/additives	1600	2300	800	22	1.25	0.011
AP/HTPB/Al	1750	3050	950	26	1.21	0.011

^a Al, aluminum; AP, ammonium perchlorate; CTPB, carboxy-terminated polybutadiene; EPON, epoxy resin; HTPB, hydroxyl-terminated polybutadiene; NC, nitrocellulose; NG, nitroglycerine; PBAA, polybutadiene-acrylic acid polymer; PBAN, polybutadiene-acrylic acid-acrylonitrile terpolymer; PS, polysulfide; PU, polyurethane

^b 6.89 MPa chamber pressure; values are typical, although may vary depending on the given propellant formulation

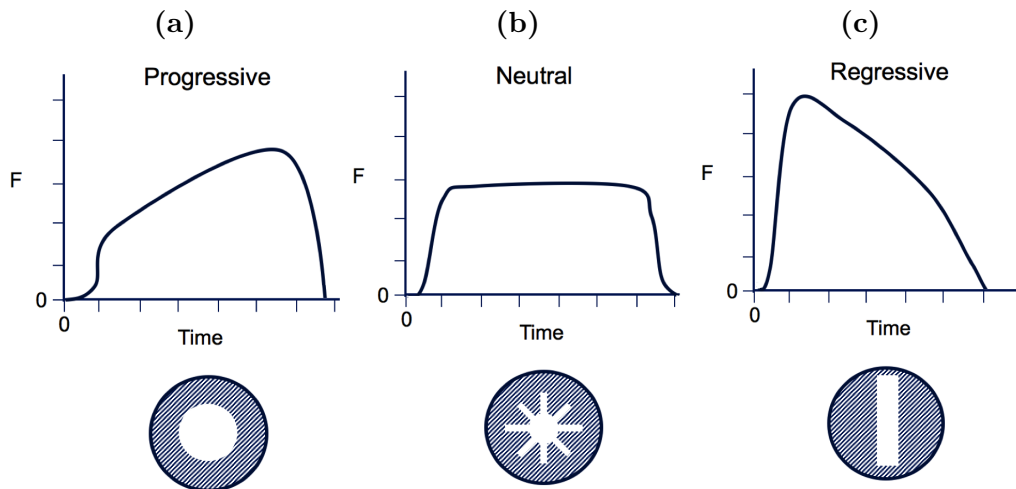
Figure 1.1: Structural features found on solid rocket motors



peratures for the entire duration of the mission, unless the motor burn duration is very short or the case is unusually robust or well insulated, the motors are usually manufactured with a central hollow core and the propellant burns from the inside outward. The amount of thrust available at any particular point in the firing of an SRM is highly dependent on the exposed area of propellant surface burning at that point in time. Various central core geometries allow different thrust profiles to be created, some examples of which are shown in Fig. 1.2.

During firing, the burning surface is regressing (as ambient-temperature propellant is converted into the high-temperature, high-pressure gas and combustion by-products of deflagration) in a direction normal to the burning surface. A cylindrical core perforation will gradually expose more propellant surface area and as shown in Fig. 1.2a the instantaneous thrust will increase during the duration of the burn.

Figure 1.2: Thrust profiles from various grain geometries

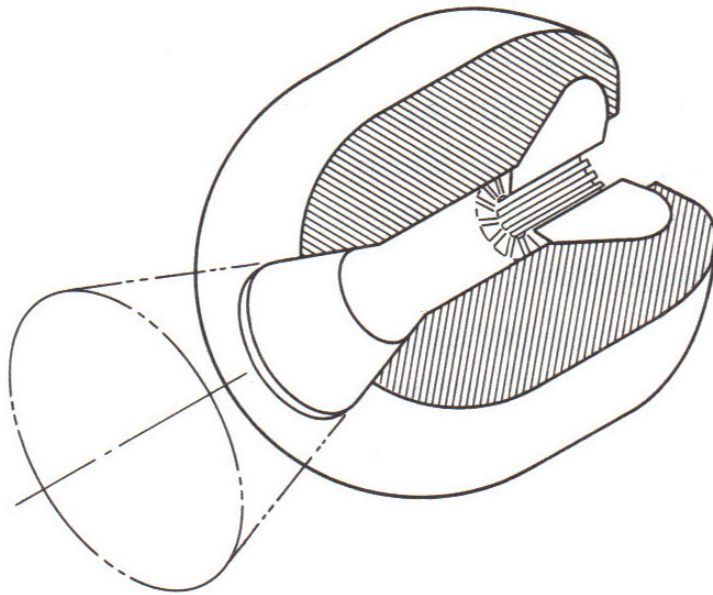


This is not always desirable because at the same time that thrust is increasing the mass of the flight vehicle is decreasing (as propellant is burned away) so the longitudinal acceleration on the flight vehicle increases significantly. In addition, the simple cylindrical core has the lowest burning surface area (and lowest thrust) right after ignition when conversely one would commonly want the most thrust early on.

The star grain profile as shown in Fig. 1.2b has a number of fins or slots (typically) molded into the propellant grain, giving a larger surface area available at the beginning of the firing which contributes to a high initial thrust, but then as the web of the star grain is consumed, the core starts to evolve towards a cylindrical shape. By carefully matching the size and length of the star grain profile to the burn rate of the propellant, a flat or neutral thrust-time curve can be produced. It is also quite common to have only one part of the fuel grain molded with extra propellant surface-exposing fins or slots, with the remainder a simple cylindrical bore. Such

configurations are called *finocyl* (fin + cylinder) and are often found in the upper-stage motors of multi-stage launch vehicles [1], providing a neutral thrust profile especially in SRM casing designs which are not cylindrical as shown in Fig. 1.3 [2].

Figure 1.3: Cutaway diagram of a finocyl propellant grain in an SRM showing the combination of a cylindrical central port and a star grain plus radial slots or fins cast into the forward section of the propellant grain



Finally, the third profile in Fig. 1.2c features a slot profile which will give a fairly high initial surface area but as the firing progresses, the propellant area is reduced and the thrust profile shows a regressive curve. Such a thrust profile provides a high initial thrust to quickly accelerate the flight vehicle at launch and then the regressive thrust curve combines with the steady reduction in propellant mass over the duration of the firing to produce a more neutral acceleration curve.

In all cases shown this far, the thrust profile is fixed at the time of SRM manufacture or assembly but, because of real-time requirements (e.g. last minute payload changes, maneuvering requirement, interception), it is desirable on occasion that the SRM thrust be able to be modulated on command during parts of the flight. The remainder of this thesis will examine the factors that affect the instantaneous propellant burning rate, investigate various ways to modify that burning rate, and compare and contrast some of the design and engineering tradeoffs between the two techniques that one may consider for thrust modulation.

2 Solid Propellant Burning Rate Models

The thrust of any chemical rocket can be ideally calculated by [1]

$$F = \dot{m}_e u_e + (p_e - p_\infty) A_e \quad (2.1)$$

Assuming that the nozzle is choked and that no mass injection occurs, from gas dynamics the mass flow through the exit of the nozzle is the same as the mass flow through the exhaust nozzle throat as described by

$$\dot{m}_t = \dot{m}_e = \left[\frac{\gamma}{RT_F} \left(\frac{2}{\gamma + 1} \right)^{\frac{\gamma+1}{\gamma-1}} \right]^{1/2} A_t p_c \quad (2.2)$$

From this equation we can see that if the nozzle throat area A_t is reduced and the mass flow remains the same, the chamber pressure p_c will inevitably increase. From the base pressure-dependent burning rate of the propellant, r_p , and the propellant solid density, ρ_p , the instantaneous mass flow rate \dot{m}_e in this simplified scenario can also be determined by

$$\dot{m}_e = r_p \rho_p S_p \quad (2.3)$$

where S_p is the area of the burning propellant surface. It is also possible to calculate the motor thrust with an ideal or underexpanded choked nozzle directly from the ratio of the chamber pressure and the nozzle exit pressure p_e via

$$F = C_{F,v} \left[1 - \left(\frac{p_e}{p_c} \right)^{\frac{\gamma-1}{\gamma}} \right]^{1/2} A_t p_c + (p_e - p_\infty) A_e \quad (2.4)$$

where $C_{F,v}$ is the vacuum coefficient of thrust as calculated by

$$C_{F,v} = \left[\frac{2\gamma^2}{\gamma-1} \left(\frac{2}{\gamma+1} \right)^{\frac{\gamma+1}{\gamma-1}} \right]^{1/2} \quad (2.5)$$

which is a function of the gas ratio of specific heats of the combustion gases [1].

The performance of a solid rocket motor is initially dependent on the nominal or base pressure-dependent burning rate r_p of the propellant composition itself but this burn rate can be influenced in various other ways during the firing cycle. It is well known [1, 3, 4, 6, 8] that the burning rate of solid rocket propellant is affected by the following three factors:

1. Chamber pressure (pressure-dependent burning)
2. Axial mass flux (erosive burning)
3. Normal acceleration

2.1 Pressure Dependent Burning

The burning rate r_p of most solid propellants exhibits a dependence on the local static pressure, governed by de St. Robert's or Vieille's empirical law [1]:

$$r_p = Cp^n \quad (2.6)$$

where C and n are determined empirically by various test firings at different chamber pressures p_c . The exponent n is in the range of 0.2 to 0.5 and coefficient C is sensitive to the propellant's initial starting temperature T_i :

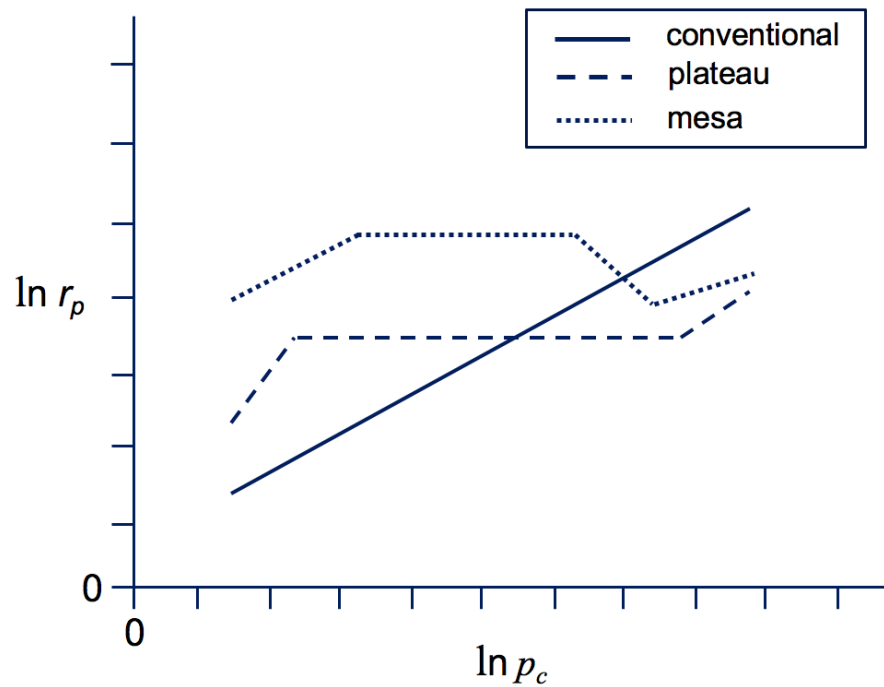
$$C = C_o \exp[\sigma_p (T_i - T_{io})] \quad (2.7)$$

where C_o and T_{io} are at reference conditions, for example, standard sea-level values, and σ_p is the pressure-dependent burning-rate temperature sensitivity coefficient, which can range from 0.001 to 0.009 K⁻¹. Initial starting temperatures significantly below nominal for the propellant formulation will reduce C and therefore lead to a reduction in r_p which can result in a lower chamber pressure p_c , potentially leading to combustion instabilities and reduced thrust [1].

For conventional propellants, plotting burning-rate versus chamber pressure results in a straight line profile on a log-log graph as show in Figure 2.1. The pressure-dependent burning-rate behaviour for other solid propellant categories can be different from the conventional profile. Some propellants can display a plateau characteristic where the burning rate remains relatively constant over a range of pressures.

Others display a mesa profile where the burning rate can initially rise and remain steady like a plateau-type propellant before exhibiting a decrease in burn rate while the chamber pressure continues to increase. The investigations in this thesis will focus on propellants exhibiting conventional pressure-dependent behaviour.

Figure 2.1: Pressure-dependant burning rate behaviour of three propellant categories



2.2 Erosive Burning

Positive erosive burning is an augmentation of the base burning rate due to the heightened convective heat transfer from the predominantly turbulent flow over the burning surface of the propellant [1]. The erosive burning component r_e can be

estimated from the Greatrix and Gottlieb convective heat transfer feedback model [1, 3, 8]:

$$r_e = \frac{h(T_F - T_s)}{\rho_s [C_s(T_s - T_i) - \Delta H_s]} \quad (2.8)$$

where the convective heat transfer coefficient h under transpiration, assuming turbulent flow corrected for compressibility, is described by

$$h = \frac{\rho_s r_b C_p}{\exp\left(\frac{\rho_s r_b C_p}{h^*}\right) - 1} \quad (2.9)$$

with h^* calculated as a function of the zero-transpiration Darcy-Weisbach friction factor f^* and axial mass flux G from

$$h^* = \frac{k^{2/3} C_p^{1/3} G f^*}{\mu^{2/3} 8} \quad (2.10)$$

where the value of f^* may be found for fully developed turbulent flow using Colebrook's expression

$$(f^*)^{-1/2} = -2 \log_{10} \left[\frac{2.51}{\text{Re}_d (f^*)^{1/2}} + \frac{\epsilon/d_p}{3.7} \right] \quad (2.11)$$

In some experiments, the burning rate appears to drop below the expected value at lower flow speeds and recover at higher core flow speeds. This effect is known as negative erosive burning and Greatrix [1] has proposed that this phenomenon may be due to laminar-type stretching of the of the effective combustion zone height with the local core flow as shown in Fig. 2.2. Extending Eq. 2.8 to include the burning rate

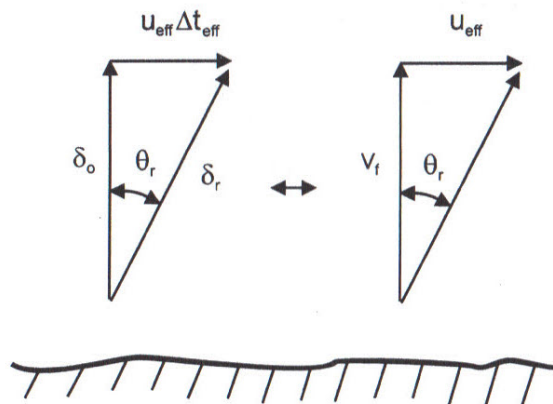
reduction caused by this stretching of the combustion zone height gives an overall burning rate of

$$r_b = \left. \frac{r_b}{r_o} \right|_{\delta_r} \cdot r_o + r_e \quad (2.12)$$

where via Greatrix's analysis [1]:

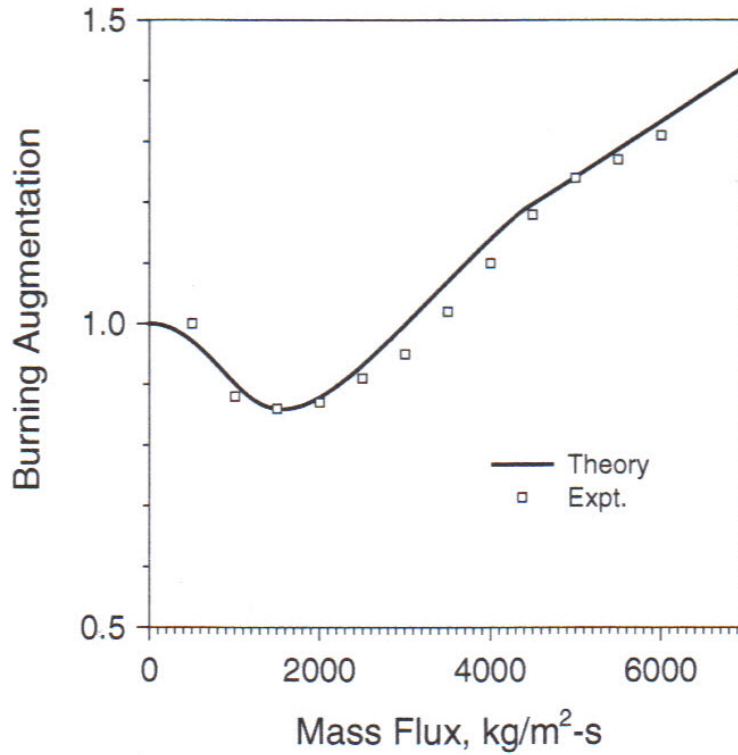
$$\left. \frac{r_b}{r_o} \right|_{\delta_r} = \cos \left[\tan^{-1} \left(\frac{u_{eff}}{v_f} \right) \right] = \cos \left[\tan^{-1} \left(K_\delta \delta_o \left[1 - (f/f_{lim})^{1/2} \right] \frac{\rho u_\infty}{\rho_s r_o} \right) \right], f < f_{lim} \quad (2.13)$$

Figure 2.2: Schematic diagram of combustion zone stretching



In this case, δ_r is the effective thickness of the stretched combustion zone under core flow relative to the base thickness δ_o under pressure-dependent burning only. Fig. 2.3 is an example of this negative erosive burning effect manifesting early in the firing while the flow speed within the core is fairly low and the flow is laminar [1]. The effect appears to largely disappear at higher flow speeds as the flow becomes more turbulent and positive erosive burning dominates.

Figure 2.3: Theoretical and experimental data for burning rate augmentation as a function of mass flux



2.3 Acceleration Effects on Burning Rate

Due to radial vibration or spinning along the SRM's longitudinal axis, normal acceleration a_n may act to augment the burning rate of the solid propellant [13–15, 17, 22, 23]. Greatrix [1, 3, 6] has put forward a generalized model that represents the combustion zone as being compressed (i.e. the effective flame height is reduced) under a normal acceleration field. This compression results in an augmentation of

the propellant burning rate according to

$$r_b = \left[\frac{C_p (T_F - T_s)}{C_s (T_s - T_i) - \Delta H_s} \right] \frac{(r_b + G_a / \rho_s)}{\exp [C_p \delta_o (\rho_s r_b + G_a) / k] - 1} \quad (2.14)$$

The base combustion zone thickness δ_o can be estimated from

$$\delta_o = \frac{k}{\rho_s r_o C_p} \cdot \ln \left[1 + \frac{C_p (T_F - T_s)}{C_s (T_s - T_i) - \Delta H_s} \right] \quad (2.15)$$

where r_o is the base burning rate resulting from pressure dependent and erosive burning effects. For a given propellant, the burning rate augmentation is related to increasing a_n as show in Fig. 2.4 [1]. The accelerative mass flux G_a is determined by a_n and the corresponding reduction of that augmentation comes through lateral or longitudinal acceleration, moving the resultant acceleration vector away from the reference orientation angle of zero (perpendicular to surface) to some finite value [6] determined from

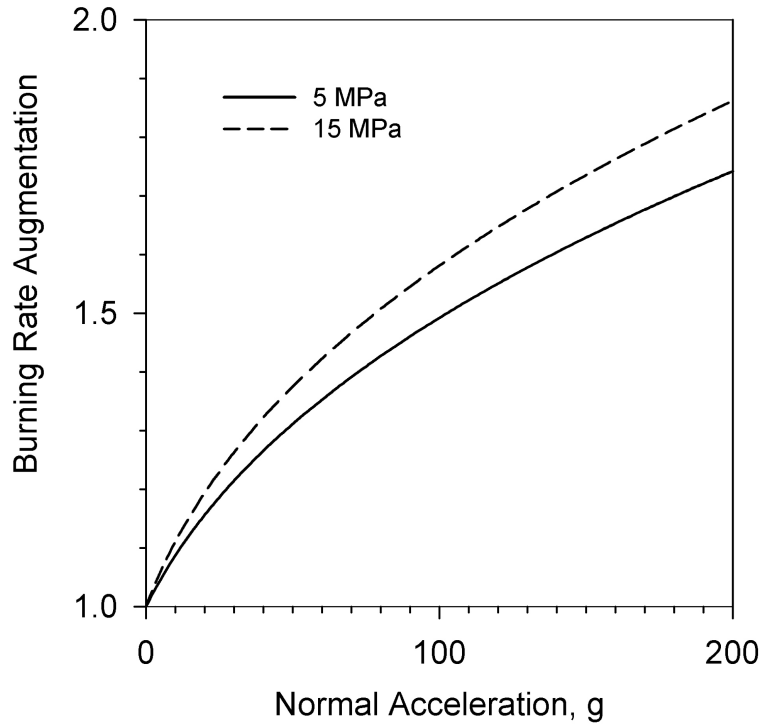
$$G_a = \left\{ \frac{a_n p}{r_b} \frac{\delta_o}{RT_f} \frac{r_o}{r_b} \right\}_{\phi=0^\circ} \cos^2 \phi_d \quad (2.16)$$

The displacement orientation angle ϕ_d is a function of ϕ , reflecting the increased reduction in augmentation that one observes experimentally as ϕ increases can be calculated as

$$\phi_d = \tan^{-1} \left[K \left(\frac{r_o}{r_b} \right)^3 \tan \phi \right] \quad (2.17)$$

where correction factor K has been experimentally determined to be approximately

Figure 2.4: Burning rate augmentation of AP/PBAA solid propellant as a function of normal acceleration at two different pressures

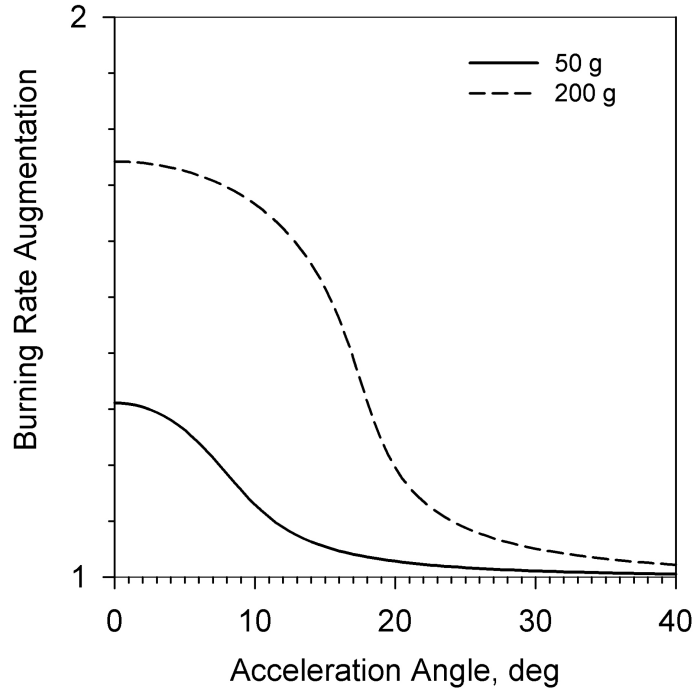


8 [1] and ϕ as shown in Fig. 3.3 is calculated as

$$\phi = \tan^{-1} \left(\frac{a_l}{a_n} \right) \quad (2.18)$$

where a_l and a_n are the longitudinal and normal accelerations. The predicted effect of decreasing burning rate augmentation due to normal acceleration as orientation angle ϕ increases due to increasing longitudinal acceleration a_l is shown in Fig. 2.5 [1, 6].

Figure 2.5: Burning rate augmentation of AP/PBAA solid propellant as function of resultant acceleration angle, at two different a_n levels (at 5 MPa pressure).



In practice, in a free flight situation, the rocket vehicle (and the motor within) will likely be undergoing significant forward longitudinal acceleration with the application of additional thrust at some point in a flight mission. This forward acceleration of the vehicle is the effective a_l acting to potentially reduce the effect of spin-induced normal acceleration on the solid propellant's burning process, as per Eq. 2.17. From reference [9], presented as an earlier part of this thesis study, an example of this influence is shown in Fig. 2.7, with a constant a_l of 15 g being applied during the spin period. Comparing the baseline case of Fig. 2.6 and the 15 g case of Fig. 2.7,

one can see a significant reduction in the spin-induced chamber pressure buildup. The result is consistent with a mean acceleration orientation angle of around 10° (see Fig. 2.5). The corresponding sea-level thrust-time profile under a 15 g forward acceleration is provided in Fig. 2.8.

Figure 2.6: Head-end pressure-time profiles of AP/PBAA solid rocket motor, baseline case, and manoeuvring case with 20 rps spin, $3 \text{ s} < t < 4.5 \text{ s}$, and zero longitudinal acceleration

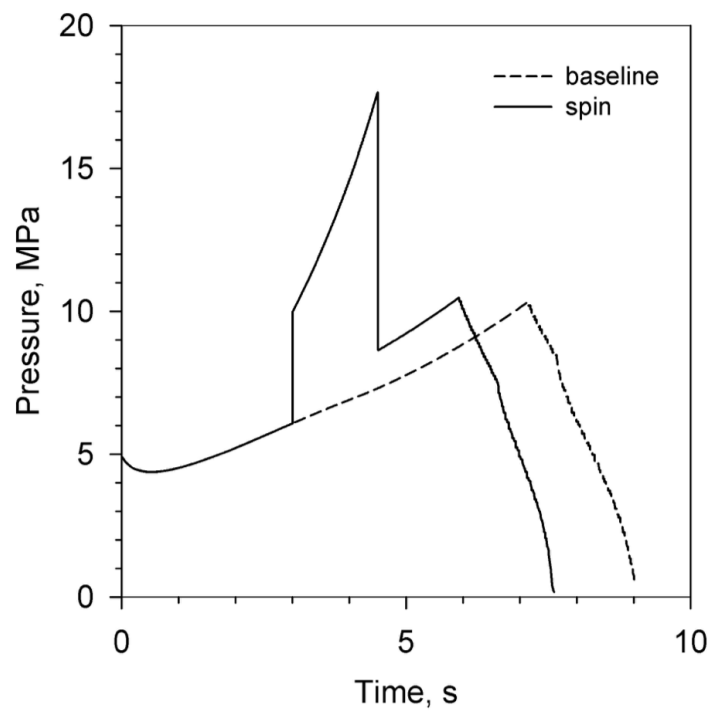


Figure 2.7: Head-end pressure-time profiles of AP/PBAA solid rocket motor, baseline case, and manoeuvring case with 20 rps spin, $3 \text{ s} < t < 4.5 \text{ s}$, and 15 g longitudinal acceleration

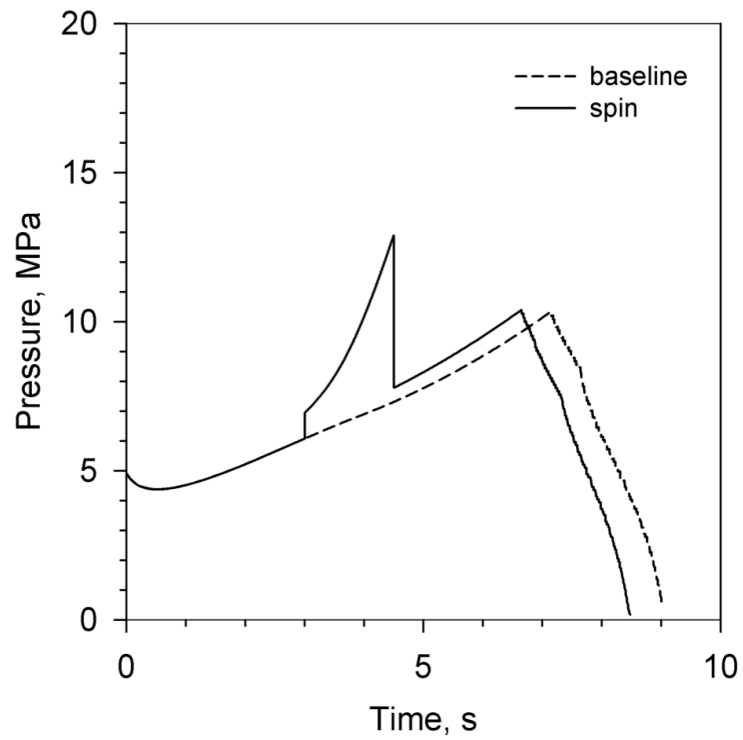
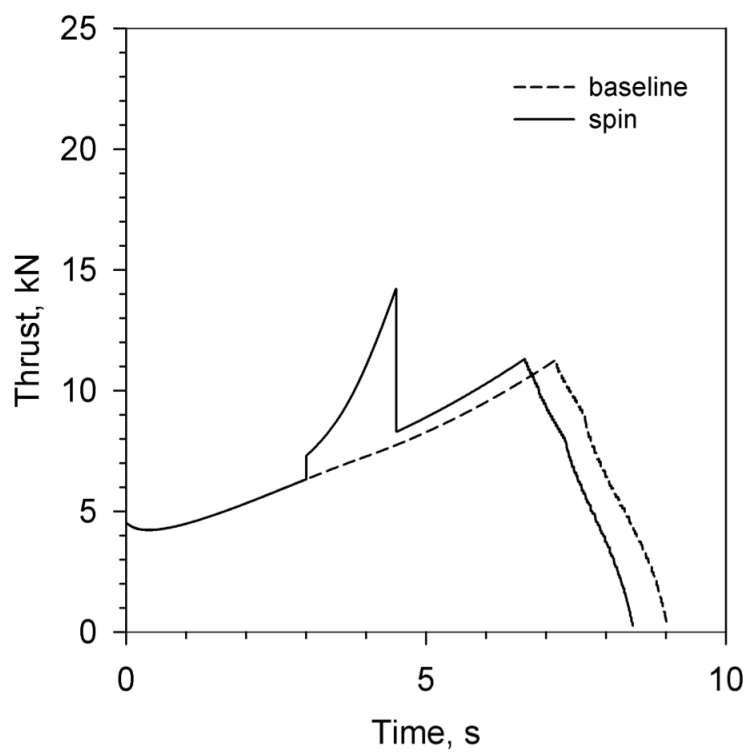


Figure 2.8: Sea-level thrust-time profiles of AP/PBAA solid rocket motor, baseline case, and manoeuvring case with 20 rps spin, $3\text{ s} < t < 4.5\text{ s}$, and 15 g longitudinal acceleration



3 Thrust Modulation of Solid Rocket Motors

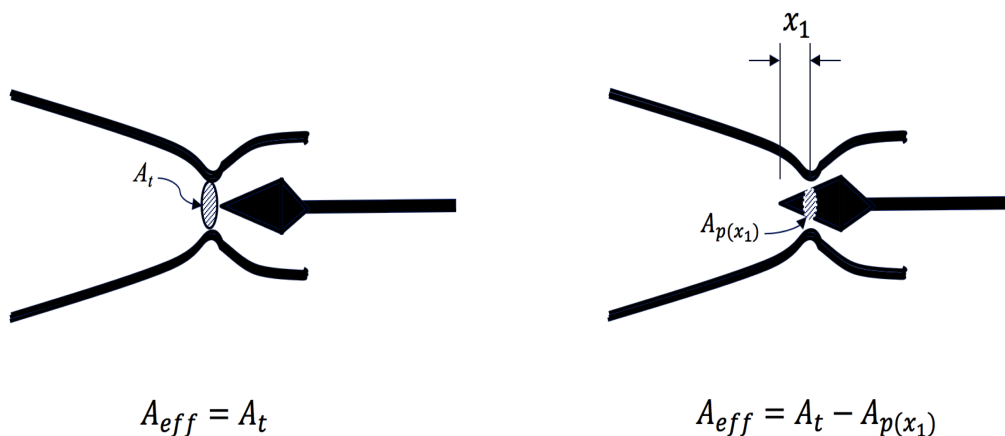
As already presented, there are a number of mechanisms governing the solid propellant burn rate. By dynamically adjusting one of these mechanisms, the thrust of the SRM may be adjusted over the baseline thrust profile. Historically, methods to increase the chamber pressure have been used, but these methods only increase the thrust modestly at the expense of very high chamber pressures and momentum losses due to obstructions in the gas flow. An alternative strategy, employing normal acceleration to vary the thrust produced by the motor, will be described in this section. A comparison of this novel approach will be made with the conventional approach of using a pintle (i.e. variable throat area) nozzle.

3.1 Burning Rate Augmentation Due to Increased Chamber Pressure

To modulate the thrust being delivered from an SRM, one or more of the burning rate mechanisms would have to be dynamically modified during the operation of the motor. For pressure-dependent burning, this is commonly done by varying the throat area of the convergent-divergent nozzle using a moveable plug called a pintle

as shown in Fig. 3.1 [10]. Moving the pintle towards the nozzle throat reduces the cross-sectional area of the throat. The pintle is operated hydraulically, pneumatically, or electrically as commanded by the flight control system.

Figure 3.1: Moveable pintle varying the throat area of the nozzle



The effective area of the nozzle throat A_{eff} is found by subtracting the area of the pintle at a particular extended position x_1 from the base area of the throat when the pintle is fully retracted. From Eq. 2.2, by reducing the cross-sectional area of the nozzle throat, the chamber pressure will be increased. This increased chamber pressure will increase the propellant burning rate via Eq. 2.6 and from Eq. 2.3, increasing the propellant burning rate will increase the mass flow which therefore via Eq. 2.1 increases the thrust. From Heo [10] it was observed that in many of the studies that complicated shock waves and flow separation in the pintle nozzle occurred around the nozzle and that these induced interference phenomena, turbulence, and flow instability.

3.2 Burning Rate Augmentation Due to Normal Acceleration

The propellant burning rate can be influenced by establishing a normal acceleration field to the burning surface. This can be done by spinning the rocket on its longitudinal axis as shown in Fig. 3.2. In 1965, Bastress [11] developed a theoretical model that predicted that the burn rate augmentation experienced in a spinning SRM was due to an effective reduction in throat area as a result of the tangential velocity imparted to the central gas flow. A later experimental study by Broddner [16] in 1970 compared a spinning rocket engine with a conventional single central nozzle and one with multiple peripheral nozzles (to cancel out the effective throat reduction effect due to spin-induced vortex flow). It was concluded that in the latter case a burning rate increase was noted due to the normal acceleration effects alone. It should be noted that in the Broddner experiments, very high rotational velocities were used to establish the spin-induced nozzle-area reductions and normal accelerations to the propellant burning surface, in excess of 11,000 rpm (over 180 rotations per second).

Figure 3.2: SRM spinning as a means of inducing a normal acceleration field

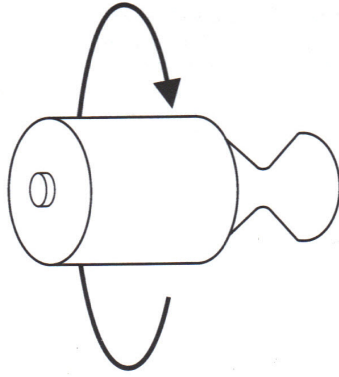
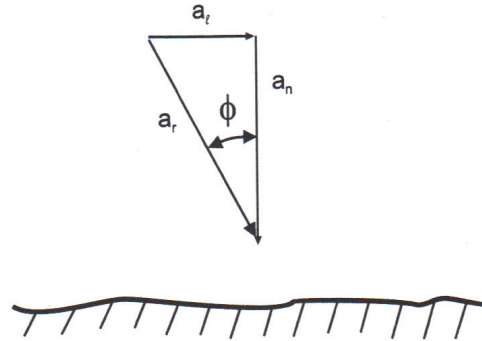


Figure 3.3: Schematic diagram of acceleration vectors acting near the propellant surface



3.3 Acceleration Effects in Metallized and Non-Metallized Propellants

With regards to the effect of a normal acceleration field on metallized and non-aluminized propellants as discussed by Glick [12], Northam [18], Crowe [19] and Fuchs [20], it was hypothesized that metallized propellants (that is, propellants that contain a quantity of metal particles as fuel or as combustion modifiers) should respond differently to a normal acceleration field than non-metallized ones. For metallized propellants, the studies theorized that this would be due to the metal particles being held closer to the propellant burning surface for a (relatively) longer period of time due to the normal acceleration, and that this results in an increased heat transfer to the fuel grain which increases the burning rate. For non-metallized propellants, the same study suggested that there was little burning rate response

to acceleration fields under 100 g and using a granular diffusion flame model, the burning rate increase is predicted to be due to the effect of the acceleration field on the heterogeneous structure of the gas phase reaction zone.

These early efforts were not consistent with the empirical results of the time (e.g. some high-percentage metallized propellants saw less burning-rate augmentation than lower percentage propellants [20]) and relied on experimentally determined coefficients [4] which made it difficult to generalize the analytical models for broader engineering applications. Greatrix [1, 4, 9] took a different approach to modelling the physics underlying the phenomenon. In this later work, it was suggested that the effect of spinning on the rate of combustion was due to a compressed combustion zone (reduced flame height) under a normal acceleration field and that this was the dominant effect for the burning rate augmentation seen in spinning solid rocket motors. This model agrees well with experimental data [4, 6] for non-metallized fuels and reasonably well for a number of metallized fuels for different metal particle loading conditions. It is important to know that the Greatrix model concurs with experimental observations, in that a higher augmentation is likely to be seen with lower base burning rate propellants.

3.4 Effects of Orientation Angle on Acceleration Effects

The Glick, Northam and Greatrix studies also highlighted the idea that the burn rate augmentation effect is dependent on the orientation angle that results from

the combination of the normal acceleration a_n and any longitudinal acceleration a_l affecting the SRM at the same time. Increasing values of the total longitudinal acceleration displacement angle decrease the accelerative mass flux and therefore the burning rate augmentation. Investigations by King [22] and Langhenry [23] suggested that the peak augmentation ratio might be governed by a simple cosine relationship

$$\frac{r_b}{r_o} = \frac{r_b}{r_o} \Big|_{\phi=0} \cos \phi \quad (3.1)$$

but it was noted by Langhenry that a much stronger reduction was occurring. Greatrix [6] surmised that the longitudinal acceleration field may create a more significant effect on the liquid-phase molecules than for the gas molecules further up the combustion zone suggesting a corrected peak accelerative mass flux as shown in Eqs. 2.16 and 2.17 noting that the burning rate augmentation due to the normal acceleration decreases dramatically when the ϕ angle (as shown in Fig. 3.3) is greater than 10° [6, 9].

It is suggested in this thesis that increasing the normal acceleration field by spinning the SRM faster may at least partially overcome the decreased burn rate augmentation due to longitudinal acceleration experienced by the SRM in flight.

4 Internal Ballistic Modelling and Analysis

Internal ballistics deals with the combustion of the propellant and internal flow within the motor. For a solid rocket motor firing, one may need to solve the conservation equations of mass, linear momentum and energy for both the particle and gas phases of the internal flow.

4.1 Equations of Motion

4.1.1 Gas Phase

For a quasi-steady state operation (no analysis of more rapid transients), the following are the one-dimensional equations for conservation of mass, momentum and energy of the core gas at a given time moving left to right from the head end of the SRM towards the nozzle [1]:

$$\frac{d(\rho u)}{dx} = -\frac{1}{A} \frac{dA}{dx} \rho u + (1 - \alpha_p) \rho_s \frac{4r_b}{d} - \left(\frac{4r_b}{d}\right) \rho \quad (4.1)$$

$$\frac{d}{dx} (\rho u^2 + p) = -\frac{1}{A} \frac{dA}{dx} \rho u^2 - \left(\frac{4r_b}{d}\right) \rho u - \rho a_l - \frac{\rho_p}{m_p} D \quad (4.2)$$

$$\begin{aligned} \frac{d}{dx} (\rho u E + u p) = & -\frac{1}{A} \frac{dA}{dx} (\rho u E + u p) - \left(\frac{4r_b}{d} + \kappa \right) \rho E \\ & + (1 - \alpha_p) \rho_s \frac{4r_b}{d} \left(C_p T_f + \frac{v_f^2}{2} \right) - \rho u a_l - \frac{\rho_p}{m_p} (u_p D + Q) \end{aligned} \quad (4.3)$$

where $E = p/[(\gamma - 1)\rho] + u^2/2$ is the total specific energy of the gas at a given location, the drag force D exerted on a particle of mean diameter d_m is

$$D = \frac{\pi d_m^2}{8} C_d \rho (u - u_p) |u - u_p| \quad (4.4)$$

and Q is the heat transfer from the gas to a given (spherical) particle is calculated by

$$Q = \pi d_m k \cdot Nu - (T - T_p) \quad (4.5)$$

4.1.2 Particle Phase

For the particle phase, the corresponding conservation equations are:

$$\frac{d\rho_p u_p}{dx} = -\frac{1}{A} \frac{dA}{dx} \rho_p u_p + \alpha_p \rho_s \frac{4r_b}{d} - \left(\frac{4r_b}{d} \right) \rho_p \quad (4.6)$$

$$\frac{d\rho_p u_p^2}{dx} = -\frac{1}{A} \frac{dA}{dx} \rho_p u_p^2 - \left(\frac{4r_b}{d} \right) \rho_p u_p - \rho_p a_l + \frac{\rho_p}{m_p} D \quad (4.7)$$

$$\begin{aligned} \frac{d\rho_p u_p E_p}{dx} = & -\frac{1}{A} \frac{dA}{dx} (\rho_p u_p E_p) - \left(\frac{4r_b}{d}\right) \rho_p E_p \\ & + \alpha_p \rho_s \frac{4r_b}{d} \left(C_m T_f + \frac{v_f^2}{2}\right) - \rho_p u_p a_l + \frac{\rho_p}{m_p} (u_p D + Q) \end{aligned} \quad (4.8)$$

4.2 Computer Modelling of Internal Ballistics

Using a variant of the QUROC numerical 1D finite-difference quasi-steady internal ballistics computer program employed at Ryerson University which solves the conservation equations for mass, momentum and energy of the internal flow of solid rocket motors, the chamber pressure of an SRM as a function of propellant burning surface area, etc., may be calculated under various conditions. From chamber pressure, the resulting thrust can be derived.

For this study, the QUROC program was modified to allow multiple changes to the nozzle diameter during the simulated firing to represent the presence of a pintle. This allowed the two thrust modulation techniques (chamber pressure induced burning rate augmentation, via pintle, and acceleration induced burn rate augmentation, via motor spin) to be compared.

4.3 Reference Motor

A summary of the reference motor parameters for the simulation runs are shown in Table 4.1. Note that the particle loading is considered small for this study's simulation runs, hence $\alpha_p \approx 0$. The solid propellant was chosen partly due to its

lower base burning rate, which allows for a higher augmentation of r_b for a given spin rate (a_n level) [5, 22].

The cylindrical propellant grain port geometry was chosen as it maximizes the augmentation of the burning rate due to normal acceleration versus non-cylindrical grain cross sections (such as star) as these introduce appreciable lateral acceleration components relative to the local propellant surface which result in a reduction in the burning rate augmentation effect [7].

Table 4.1: Summary of the reference solid rocket motor simulation parameters

Parameter	Value
Burning rate temperature sensitivity, σ_p	0.0016 K ⁻¹
Burning surface temperature, T_s	700 K
Flame temperature, T_f	2300 K
Grain diameter	0.127 m
Grain length	1.47 m
Initial grain port diameter	0.035 m
Initial propellant temperature, T_i	294 K
Nominal nozzle throat diameter	0.030 m
Nozzle exit plane diameter	0.070 m
Particle mass loading fraction, α_p	0
Propellant	AP/PBAA
Propellant density, ρ_p	1600 kg m ⁻³
Propellant mass, m_p	27.5 kg
Propellant pressure-dependent burning coefficient, C	0.000 664 m s ⁻¹ kPa ⁻¹
Propellant pressure-dependent burning exponent, n	0.25
Propellant specific heat (solid), C_s	1400 J kg ⁻¹ K ⁻¹
Ratio of specific heats, γ	1.24
Roughness height of propellant, ϵ	200 × 10 ⁻⁶ m
Specific heat of gas, C_p	1953 J kg ⁻¹ K ⁻¹
Spin rate range	10 - 22 rps
Variable throat diameter range	76 - 100%

5 Simulation Results

5.1 Reference Motor

As a reference, a baseline was established by simulating the firing of the reference motor without any nozzle or spin implementations during the firing (note: the initial ignition and filling phase of the firing is not modelled by the code), the results of which are shown in Figures 5.1 and 5.2.

For the reference motor shown, the maximum chamber pressure was 10.09 MPa and the maximum thrust was 11.11 kN which occurred just before burnout at 7.18 s into the firing after which there was a sharp decrease in chamber pressure and sea-level thrust as the last remnants of propellant are consumed and the chamber pressure reduced rapidly to local atmospheric pressure.

Figure 5.1: Chamber pressure-time profile for reference motor firing

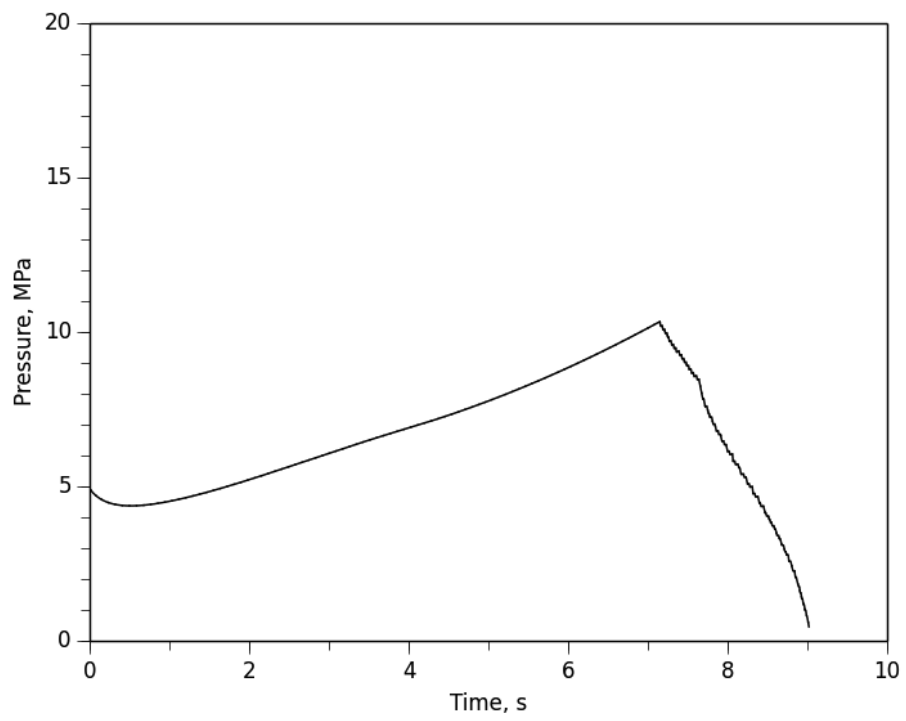
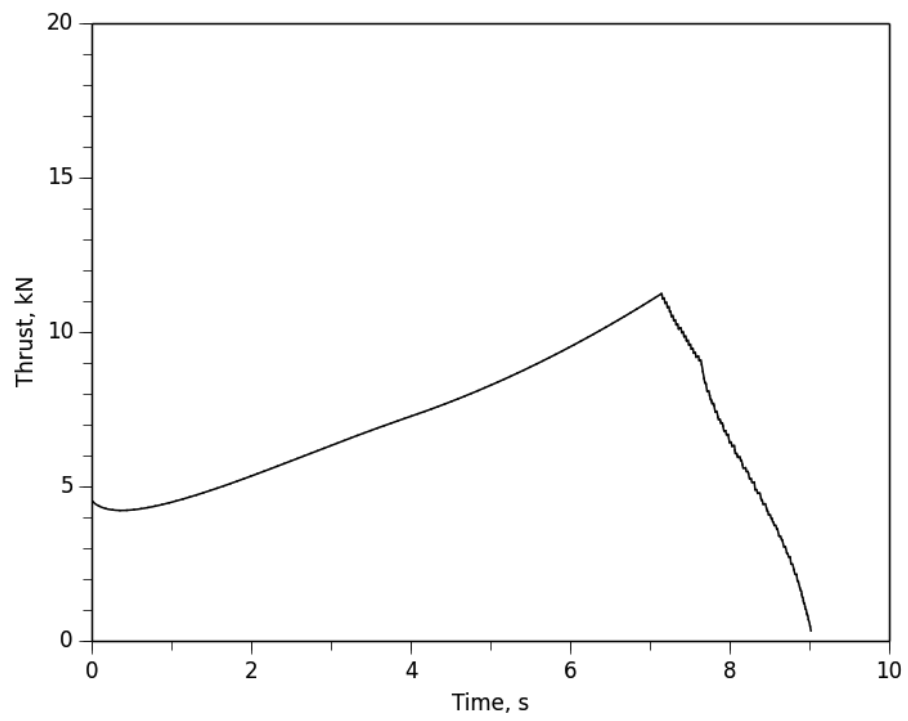


Figure 5.2: Sea-level thrust-time profile for reference motor firing



5.2 Pintle Nozzle Motor

The reference engine was again simulated but this time to simulate the use of a pintle, the nozzle throat diameter was reduced from 100% to 80% of the initial starting diameter of 0.030 m starting at 3.0 seconds into the firing. The throat diameter was further reduced at 3.75 s to 76%. At 4.5 s, the throat was opened up to 100% for the remainder of the simulated firing. The results of this simulation are shown in Figures 5.3 and 5.4.

Figure 5.3: Chamber pressure profile for pintle motor firing, 80% throat dia., $3 \text{ s} < t < 3.75 \text{ s}$, 76% throat dia. $3.75 \text{ s} < t < 4.5 \text{ s}$

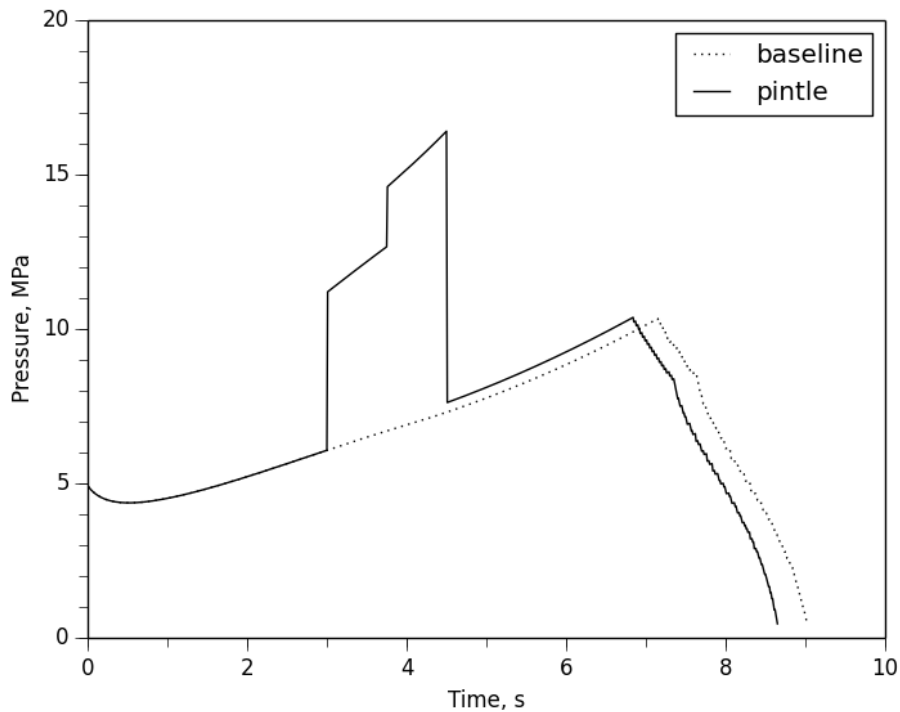
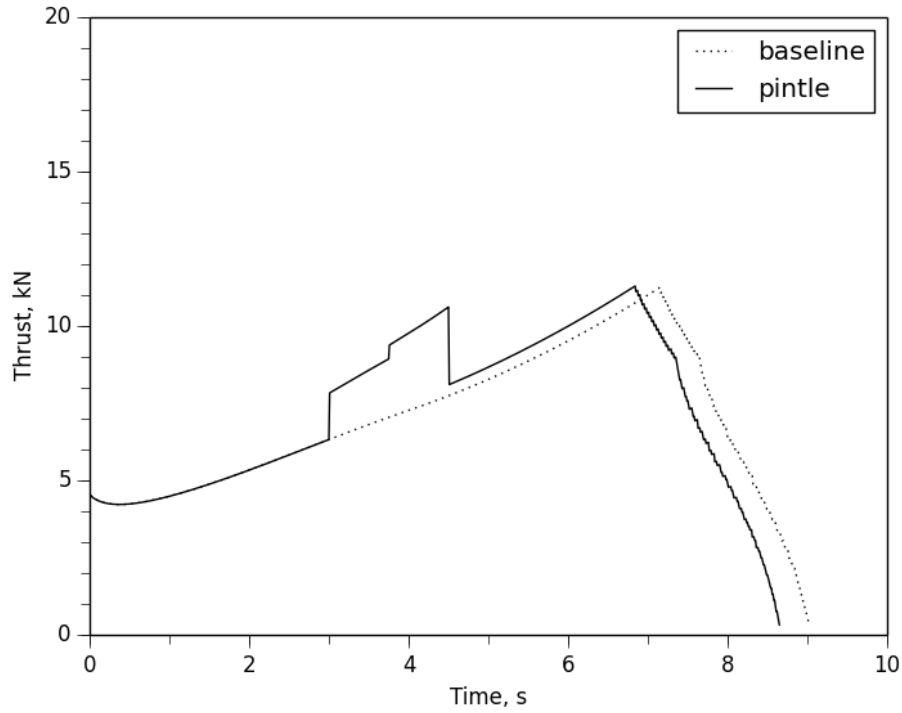


Figure 5.4: Thrust-time profile for pintle motor firing, 80% throat dia., $3 \text{ s} < t < 3.75 \text{ s}$, 76% throat dia. $3.75 \text{ s} < t < 4.5 \text{ s}$

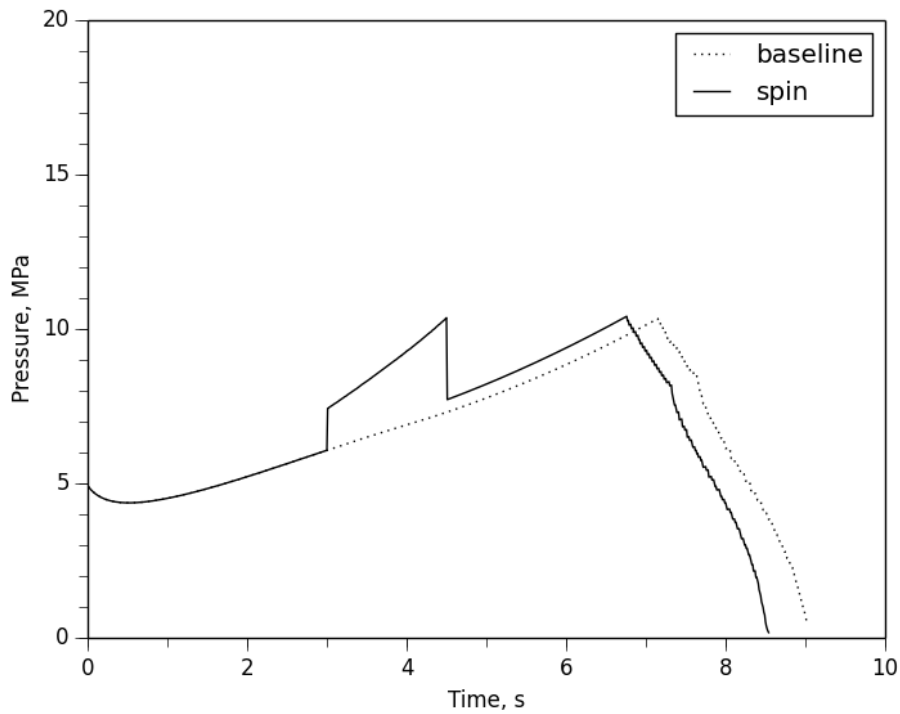


Note that because of the increased burning rate during the throat reduction period, the pintle motor does not burn as long as the reference motor. The maximum chamber pressure during the throat restriction period was 16.4 MPa and maximum thrust at the end of the period was 10.6 kN. The stepped throat diameter changes were arrived at by trial-and-error and were chosen to more closely approximate the resulting thrust curve of the spinning rocket motor simulation.

5.3 Spinning Rocket Motor

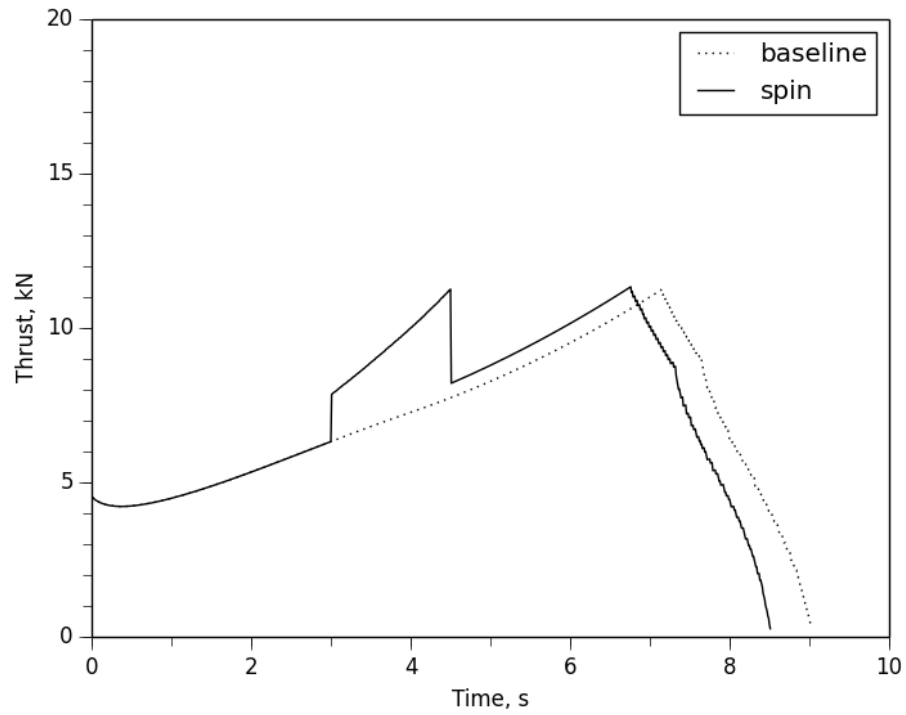
For the spinning rocket motor, the reference motor was spun at 10 rps (600 rpm) starting at 3.0 s into the firing and lasting up to 4.5 s where the rotation was stopped and the motor continued to burn as normal to end of the propellant, with the resulting pressure and sea-level thrust profiles shown in Figures 5.5 and 5.6.

Figure 5.5: Chamber pressure-time profile for spinning motor firing, 10 rps, $3\text{ s} < t < 4.5\text{ s}$



During the spinning period, the maximum chamber pressure was 10.4 MPa and the maximum sea-level thrust was 11.3 kN

Figure 5.6: Sea-level thrust-time profile for spinning motor firing, 10 rps, $3 \text{ s} < t < 4.5 \text{ s}$



5.4 Comparison of Pintle Nozzle and Spinning SRM

Figures 5.7 and 5.8 overlay both the pintle and spinning SRM pressure and sea-level thrust profiles along with the baseline generated for the reference motor.

Figure 5.7: Chamber pressure-time profiles for all motor firings

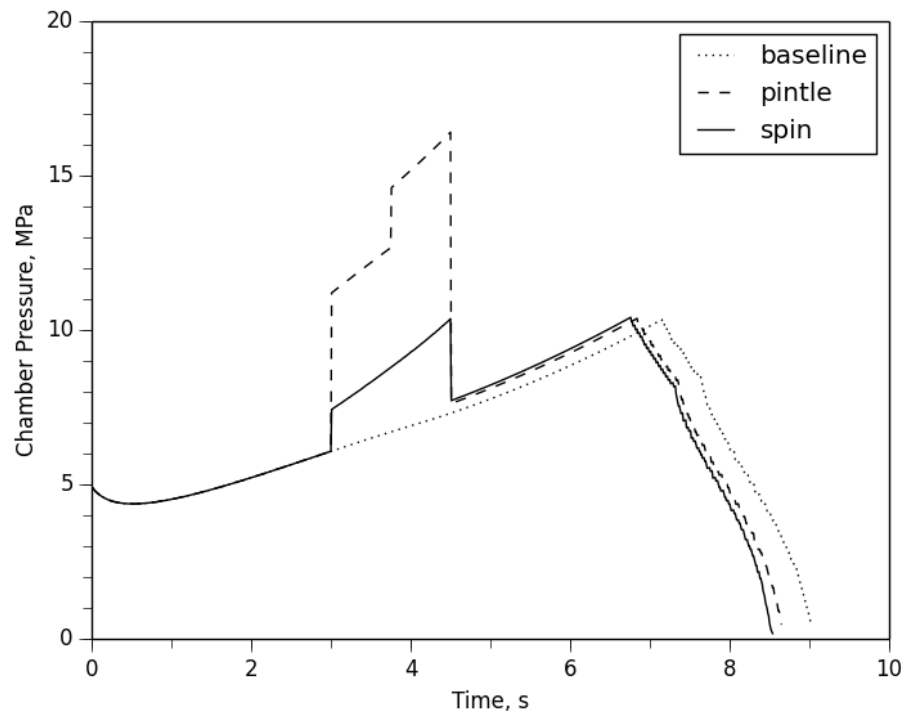
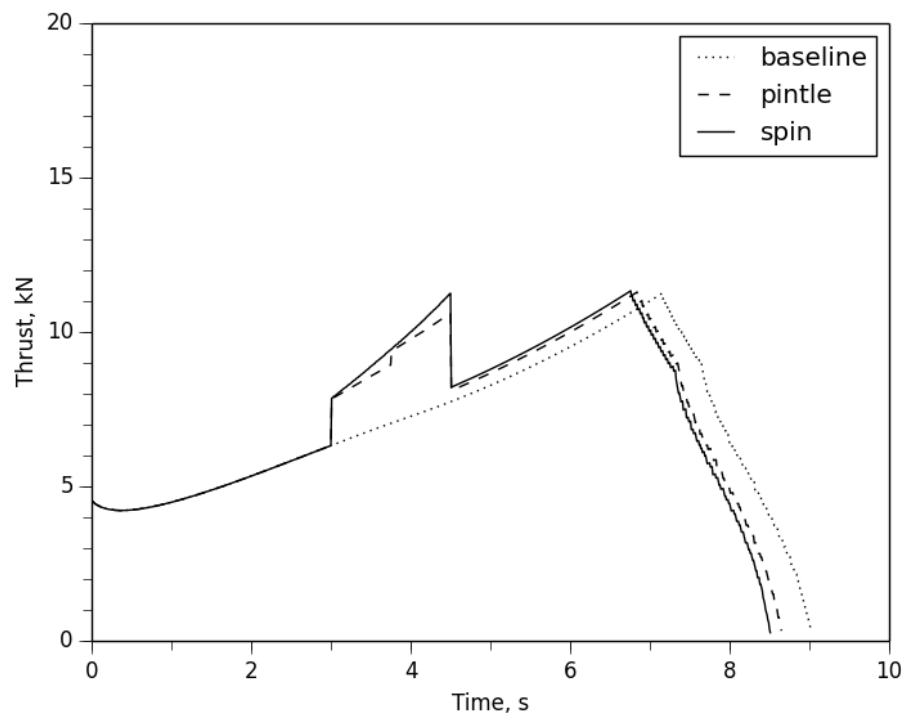


Figure 5.8: Sea-level thrust-time profiles for all motor firings



5.5 Spinning Rocket at Maximum Chamber Pressure

If one assumes for a moment that the maximum chamber pressure the reference rocket motor casing can withstand (due to material selection and thickness) is the maximum pressure generated by the pintle motor run (16.4 MPa), one can determine what the thrust generated at this pressure would be. Changing the spin rate of the motor from 10 rps to 18 rps (1080 rpm) generated the pressure and sea-level thrust profiles shown in Figures 5.9 and 5.10.

The maximum chamber pressure was 15.9 MPa and the maximum sea-level thrust was 17.8 kN during the spinning period.

Figure 5.9: Sea-level chamber pressure-time profile for spinning rocket motor, 18 rps, $3 \text{ s} < t < 4.5 \text{ s}$

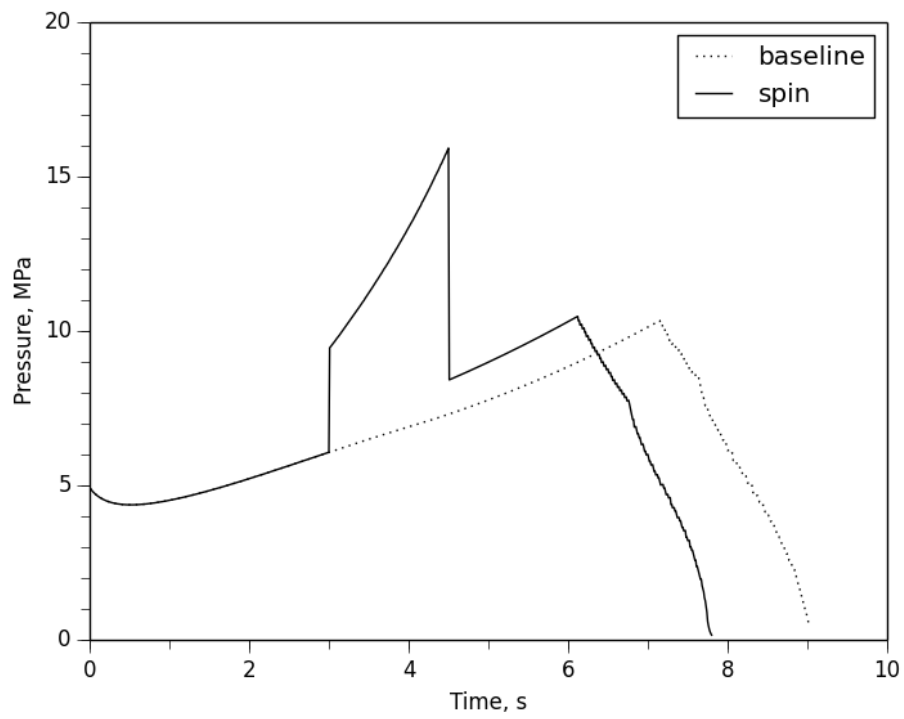
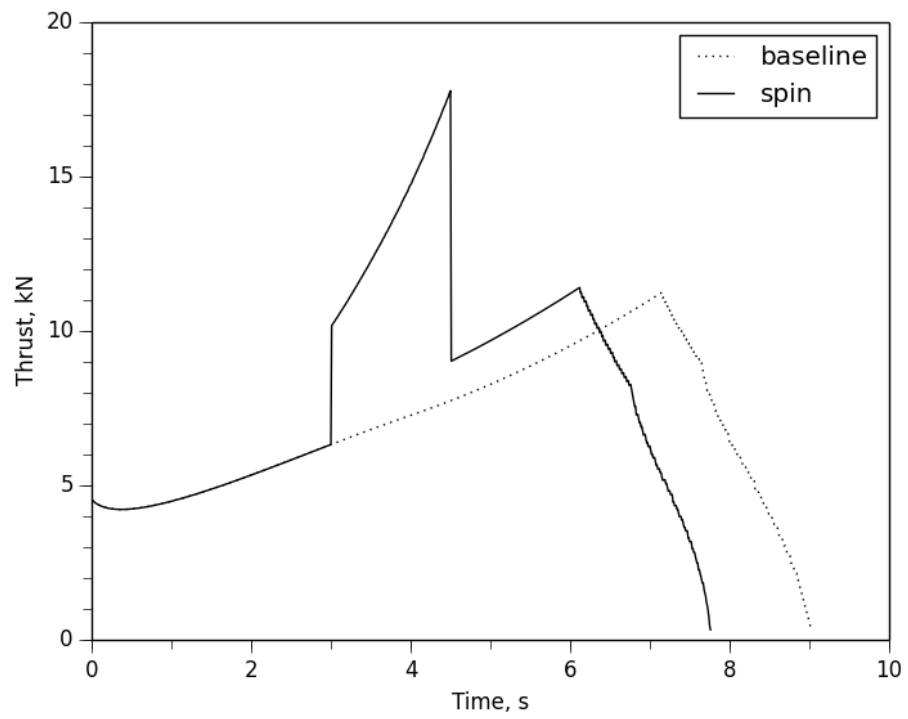


Figure 5.10: Sea-level thrust-time profile for spinning rocket motor, 18 rps, $3 \text{ s} < t < 4.5 \text{ s}$



5.6 Spinning Rocket With Longitudinal Acceleration

From Eq. 2.17 and 2.18, and Figure 2.5, it has been shown that the burning rate augmentation resulting from the normal acceleration generated due to spinning is attenuated by longitudinal acceleration which causes a resultant acceleration orientation angle in excess of 10° . The spinning rocket simulation was run again with a spin rate of 18 rps as before but, in addition, a 15 g longitudinal acceleration was applied for the duration of the firing. Figs. 5.11 and 5.12 show the resulting chamber pressure-time and thrust-time profiles for this simulation. The maximum chamber pressure attained was 9.31 MPa and the resulting maximum thrust was 10.04 kN.

To recover the thrust lost due to the longitudinal acceleration, the spin rate of the SRM was increased from 18 rps to 22 rps (1320 rpm). Figs. 5.13 and 5.14 show the chamber pressure-time and thrust-time profiles for the reference solid rocket motor with a lateral acceleration of 15 g and spinning at 22 rps. During this simulation, the maximum chamber pressure attained was 16.76 MPa and the maximum thrust generated was 18.78 kN.

Table 5.1 summarizes the chamber pressure and thrust increases recorded for each of the simulation runs. The Min/Max centripetal acceleration indicates the centripetal force based on the rate of spin for the particular simulation run at the minimum core diameter (when a_n force would be at its lowest) and what it is calculated to be at burnout (maximum core diameter) if the SRM was still spinning at the same rate (when the a_n force would be at its highest).

Figure 5.11: Sea-level chamber pressure-time profile for a spinning rocket motor, 15 g longitudinal acceleration, 18 rps, $3 \text{ s} < t < 4.5 \text{ s}$

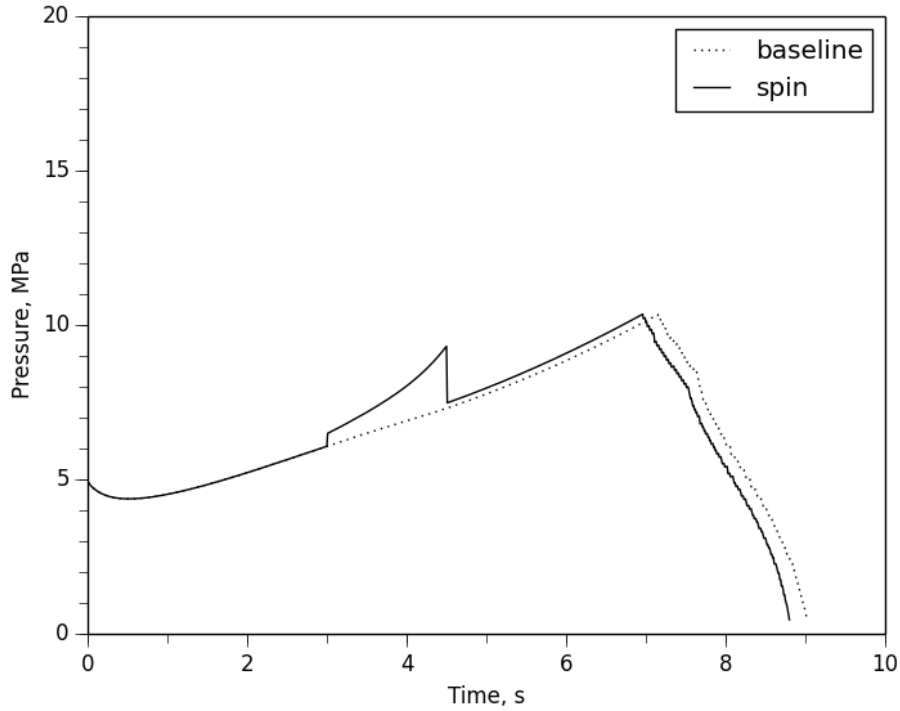


Table 5.1: Summary of the simulation results during the thrust augmentation period, $3 \text{ s} < t < 4.5 \text{ s}$

Simulation Run	Max. Chamber Pressure, MPa	Max. Thrust kN	Centripetal Accel. Min/Max, g
Baseline	10.1	11.1	n/a
Pintle	16.4	10.6	n/a
Spin, 10 rps	10.4	11.3	7/26
Spin, 18 rps	15.9	17.8	23/83
Spin, 18 rps, 15 g long. accel.	9.3	10.0	23/83
Spin, 22 rps, 15 g long. accel.	16.7	18.8	34/124

Figure 5.12: Sea-level thrust-time profile for a spinning rocket motor, 15 g longitudinal acceleration, 18 rps, 3 s < t < 4.5 s

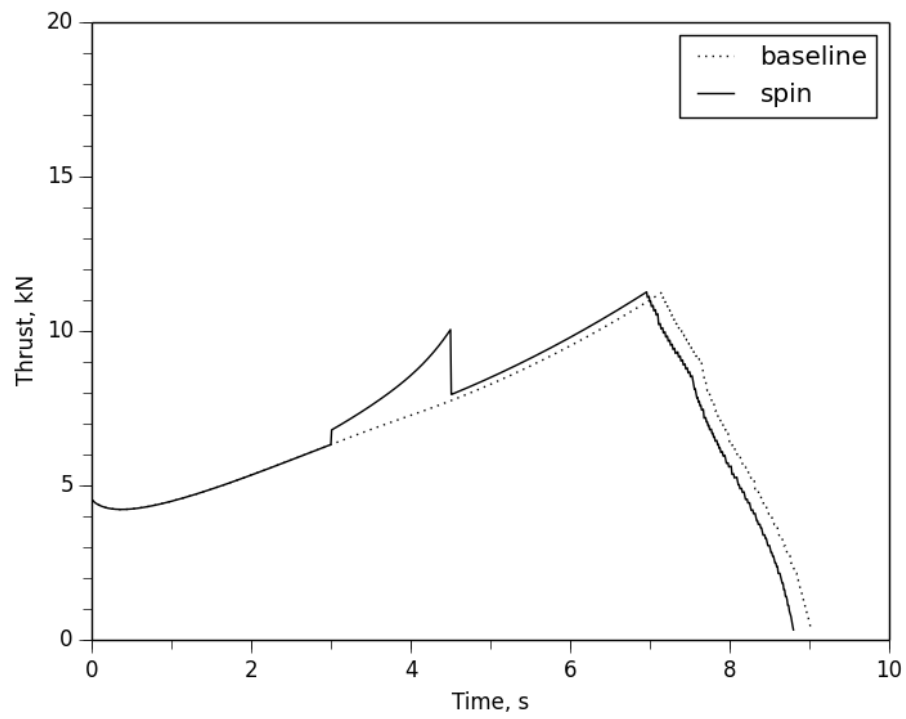


Figure 5.13: Sea-level chamber pressure-time profile for a spinning rocket motor, 15 g longitudinal acceleration, 22 rps, $3 \text{ s} < t < 4.5 \text{ s}$

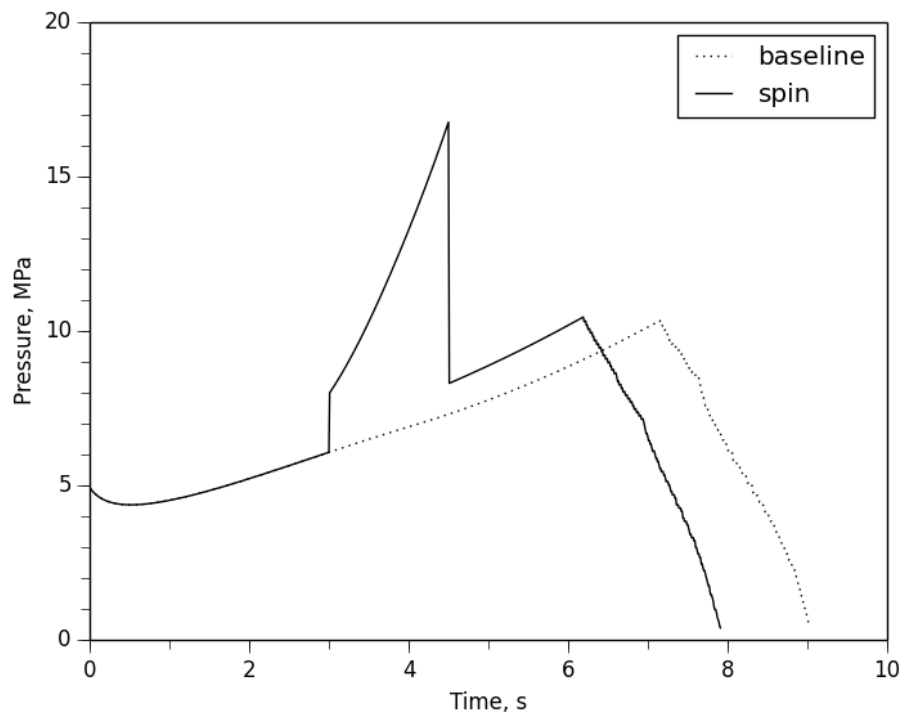
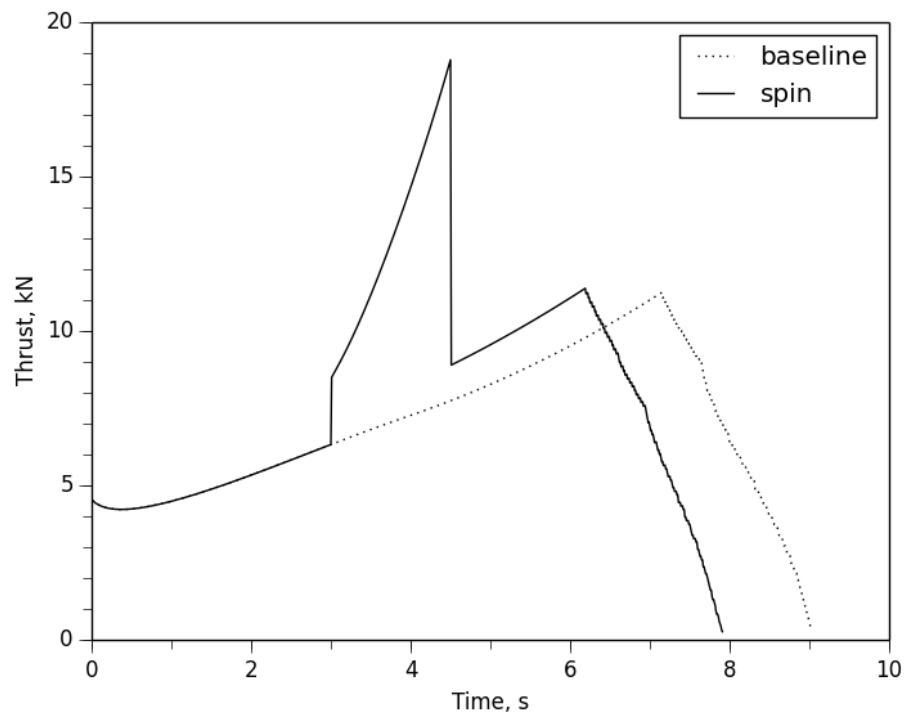


Figure 5.14: Sea-level thrust-time profile for a spinning rocket motor, 15 g longitudinal acceleration, 22 rps, 3 s < t < 4.5 s



6 Discussion of Results

Comparing the pintle-based thrust augmentation technique to one relying on spinning, for the pintle-based rocket motor, the chamber pressure rose 124% over the baseline pressure at the same point in the burn while the sea-level thrust increased 37% (Figs. 5.3, 5.4). With the spinning motor, the chamber pressure only rose 42% over the baseline pressure while the sea-level thrust increased 45% (Figs. 5.5, 5.6). The implication is that if we can achieve the same or better sea-level thrust increase via spinning than we can via the pintle design we could reduce the structural weight of the SRM casing without giving up performance.

More significant is the observation that assuming a maximum chamber pressure for the casing of 16.4MPa, we can generate a 130% increase in the sea-level thrust (17.8 kN versus 7.7 kN, Figs. 5.9, 5.10) by spinning the SRM at a modest 18 rps compared to the 37% increase available from the pintle design (10.61 kN versus 7.74 kN, Figs. 5.3, 5.4). This result suggests that there is potentially a larger range of thrust profiles available to meet mission expectations when using the spinning approach versus a pintle-based design.

In the case where the spinning flight vehicle is undergoing a substantial longitudinal acceleration, as expected we see a significant reduction in the chamber pressure and thrust generated (Figs. 5.11, 5.12). However, by modestly increasing the spin rate from 18 rps to 22 rps, the thrust augmentation is restored while staying within

the structural design limits of the rocket motor's casing (Figs. 5.13, 5.14).

Note also the rate of increase in sea-level thrust between the two approaches as shown in Figs. 5.4 and 5.6; the pintle has an almost linear thrust increase while the spinning design is much greater than linear and in Figs. 5.10 and 5.14, the curve appears to be an exponential rise. Comparing the thrust-time profile curve between spinning at 18 rps and spinning at 22 rps, we see that the slope of the thrust-curve is much steeper. This would suggest that once the SRM is set to spinning at some nominal value (say 10 or 15 rps), the thrust profile is very responsive to small adjustments to the spin rate, potentially allowing for much more aggressive maneuvers.

Note that these thrust increases do not come for free; in the 22 rps case, it can be seen that the thrust duration of the rocket motor is reduced by over a second (i.e. over 10%) in a nine-second firing. For interceptions and other critical maneuvers, this trade-off may be acceptable.

The number of g's experienced by the spinning motor is quite low; in the 10 rps case at ignition, the g-force on the inner propellant surface is on the order of 7 g and at burnout (maximum inner propellant surface radius) the theoretical maximum is 26 g according to

$$a = -\omega^2 R \tag{6.1}$$

where ω is $20\pi \text{ rad s}^{-1}$ at 10 rps and R is 0.0175 m at the start and 0.0635 m at burnout. These relatively low normal accelerations are far below those modelled by Glick [12] and investigated by Broddner [16] where the throat area was presumed to be reduced by the spin-vortex induced in the central flow. Nevertheless, even

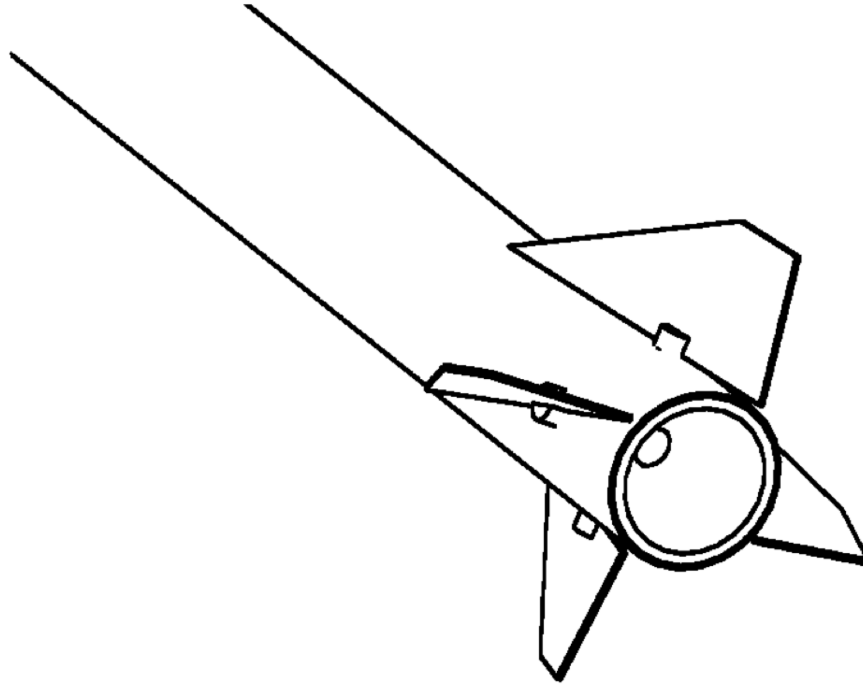
at these relatively low acceleration levels, significant thrust augmentation occurred, suggesting that nozzle throat area reductions caused by spinning are not the primary factor in the burn rate augmentation observed. Assuming the opposite for the moment, one might also expect to see the thrust-time profile similar to that of the pintle-based design whereas it can be seen from Figs. 5.6, 5.10 and 5.14 that the thrust-time profiles (especially at the higher 18 and 22 rps spin rates) are different in shape and slope from the pintle-based approach (even after accounting for the two-step pintle-based thrust curves), further suggesting that the nozzle throat area flow reductions due to spinning would not be responsible for the predicted rates of thrust augmentation.

6.1 Implementation Strategies for a Spinning SRM

There are a number of ways that an SRM in a flight vehicle could be spun during different phases of the mission or flight profile. If spinning the entire airframe is desirable (or at least not detrimental) and the demand for burning rate augmentation occurs some time after ignition, then a variable incidence fin design as shown in Fig. 6.1 could be employed to start and stop the SRM spinning once sufficient forward velocity had been achieved. The flight computer would mix the trajectory inputs and the desired spin rate to deflect the variable incidence fins as required to achieve the necessary rate of spin and attitude control.

Alternatively, instead of spinning the entire airframe, the SRM could be spun independently (i.e. the SRM is mounted in the airframe on bearings) with a suitable

Figure 6.1: Variable incident tail fins for inducing spin (shown deflected)



motor to spin and de-spin the SRM as required as shown in Fig. 6.2. In order to counteract the torque induced and to keep the airframe from spinning undesirably, variable incidence fins would also have to be employed.

Since maximum thrust is typically required at launch, another possibility is to spin the rocket up on the launch pad using an external motor as shown in Fig. 6.3. The extra weight of motor and batteries would not have to be carried as payload and there would be the added benefit of increasing the thrust at time in the mission profile where excess thrust is more desirable. This coupled with a slower regressing fuel grain would allow a solid rocket configured like this to have a higher initial

Figure 6.2: Cutaway of spinning rocket with SRM rotated independently of the airframe



thrust off the launch pad and then potentially a longer sustaining phase with the added benefit that by locking the SRM to the motor casing after launch, the launch vehicle could also benefit from variable-incidence fin induced thrust augmentation later in the flight profile. For smaller rocket airframes, the entire flight vehicle could spin within an externally driven casing from which the rocket would be launched as shown in Fig. 6.4.

Figure 6.3: Cutaway of externally spun SRM rotated independently of the airframe on the launch pad

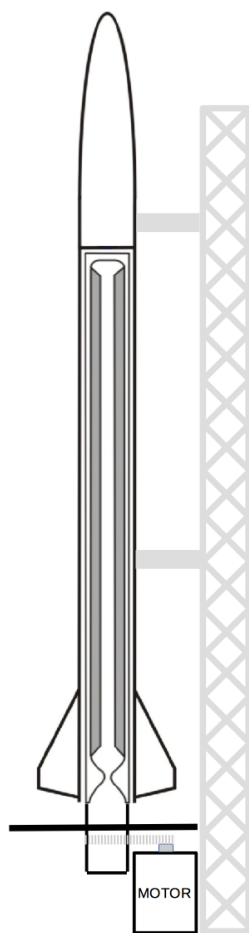
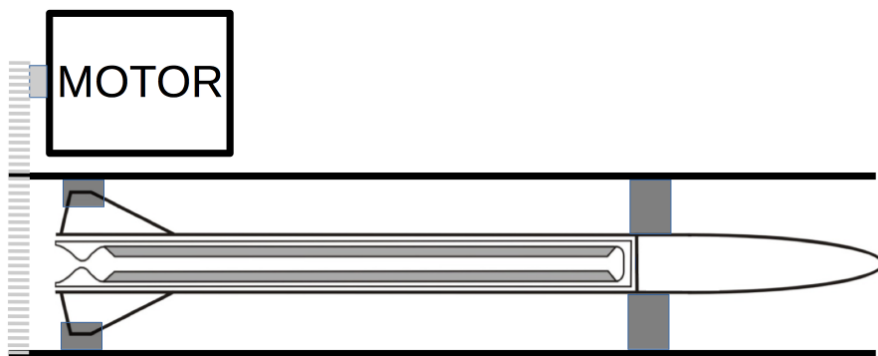


Figure 6.4: Schematic of an externally spun rocket airframe



7 Conclusion

Comparing two types of propellant burning rate augmentation approaches for SRMs, the research conducted for this thesis suggests that spinning the solid rocket motor to induce a normal acceleration results in significantly higher burning rate augmentation compared to a variable area nozzle (i.e. pintle) approach without the parallel increase in combustion chamber pressure associated with pressure-dependent burning. For a given maximum chamber pressure, the results obtained here have indicated that substantially more thrust can be derived from spinning the SRM than by using a pintle (i.e. variable area nozzle). This advantage allows higher thrust for maneuvering or interception within a given airframe, or that the airframe could be lightened significantly without loss of performance. In the event of longitudinal accelerations on the airframe causing a reduction in burn rate augmentation, the SRM can simply be spun a little faster to restore the desired level of thrust.

Various mechanisms could be employed to induce spinning in a flight vehicle, depending on where in the mission thrust augmentation was most desirable and whether or not the entire airframe or just the SRM was to be spun.

Though there have been several studies and investigations of the effects on normal acceleration of the burning rate of solid propellant rocket motors, the majority of these have been to quantify and ultimately minimize the phenomena for existing and future SRM and vehicle implementations. Additional research opportunities

exist to examine and quantify how to take advantage of normal acceleration-based burning rate augmentation and incorporate those ideas into more suitable propellant formulations for burning rate augmentation, and in turn designing solid rocket motors and flight vehicles to exploit this effect.

8 Considerations for Future Work

The research presented in this thesis could be extended in a number of significant directions. Many other types of propellants could be analyzed, as well as different sizes and lengths of SRMs to determine if there are any particular scale effects that need to be taken into consideration. A fully instrumented spinning test stand that would allow various SRM propellant compositions to be tested could be built to further generalize on the compressed combustion zone theory of burn rate augmentation. Existing off-the-shelf SRM motors could be tested as well as custom formulations. New propellant formulations especially produced for spin-augmented SRMs could be developed and tested. A small test vehicle with variable incidence fins could be constructed and flown to gather burning rate augmentation data in a real flight vehicle experiencing both normal and longitudinal accelerations and the latter's effect on the rate of augmentation (as per Figs. 2.5 - 2.8). As there has only been a small amount of work done to explore implementations of spin-augmented SRMs, there is considerable opportunity for future novel research.

References

- [1] Greatrix, D.R., *Powered Flight: The Engineering of Aerospace Propulsion*. Springer-Verlag, London Ltd, London (UK), 2012, pp. 323-343,426-427.
- [2] Sutton, G.P., *Rocket Propulsion Elements, 6th ed.* John Wiley & Sons, New York, 1992, pp. 366, 394.
- [3] Greatrix, D.R., Gottlieb, J.J., “Erosive burning model for composite-propellant rocket motors with large length-to-diameter ratios,” *Canadian Aeronautics & Space Journal*, Vol 33, pp 133-142, 1987.
- [4] Greatrix, D.R., “A Study of Combustion and Flow Behaviour in Solid-Propellant Rocket Motors,” University of Toronto, Toronto, ON, UTIAS Report No. 280, CN ISSN 0082-5255, 1987.
- [5] Greatrix, D.R., Gottlieb, J.J., “Normal Acceleration Model for Composite-Propellant Combustion,” *Transactions of the CSME*, Vol. 12, No. 4, 1988, pp. 205-211.
- [6] Greatrix, D.R., “Parametric Analysis of Combined Acceleration Effects on Solid Propellant Combustion,” *Canadian Aeronautics & Space Journal*, Vol 40, No. 2, pp 68-73, 1994.

- [7] Greatrix, D.R., "Internal Ballistic Model for Spinning Star-Grain Motors", *Journal of Propulsion and Power*, Vol. 12, No. 3, May-June 1996.
- [8] Greatrix, D.R. "Model of Prediction of Negative and Positive Erosive Burning," *Canadian Aeronautics & Space Journal*, Vol 53, 2007, pp 13-21.
- [9] Greatrix, D.R., Wozney, C., Bockelt, M., "Alternative Thrust Modulation Techniques for Solid and Hybrid Rockets," *65th International Astronautical Conference, Space Propulsion Symposium*, Toronto, ON, 2014.
- [10] Heo, J., Jeong, K., Sung, H.G., "Numerical Study of the Dynamic Characteristics of Pintle Nozzles for Variable Thrust," *Journal of Propulsion and Power*, Vol. 31, No. 1, January - February 2015, pp. 230-237.
- [11] Bastress, E. K., "Interior Ballistics of Spinning Solid-Propellant Rockets," *Journal of Spacecraft and Rockets*, Vol. 2, No. 3, May-June 1965, pp 455-457.
- [12] Glick, R.L., "An Analytical Study of the Effects of Radial Acceleration Upon the Combustion Mechanism of Solid Propellant," Thiokol Corporation, Huntsville, AL, Contract NAS7-406, 1966.
- [13] Anderson, J., Reichenbach, R., "An Investigation of the Effect of Acceleration on the Burning Rate of Composite Propellants," *AIAA Journal*, Vol. 6, No. 2, Feb.1968, pp. 271- 277.
- [14] Lucy, M.H., "Spin Acceleration Effects on Some Full-Scale Rocket Motors," *Journal of Spacecraft and Rockets*, Vol. 5, No. 2, February 1968, pp. 179-183.

- [15] Sturm, E.J., Reichenbach, R.E., “An Investigation of the Acceleration-Induced Burning Rate Increase of Non-Metallized Composite Propellants,” *AIAA Journal*, Vol. 8, June 1970, pp. 1062- 1067.
- [16] Broddner, S., “Effects of High Spin on the Internal Ballistics of a Solid Propellant Rocket Motor,” *Aeronautica Acta*, Vol. 15, 1970, pp 191-197.
- [17] Northam, G.B.and Lucy, N.H., “On the Effects of Acceleration Upon Solid Rocket Performance,” *Journal of Spacecraft and Rockets*, Vol. 6, April 1969, pp. 456-459.
- [18] Northam, G.B., “Effects of the Acceleration Vector on Transient Burning Rate of an Aluminized Solid Propellant,” *Journal of Spacecraft and Rockets*, Vol. 8, No. 11, 1971, pp. 1133-1137.
- [19] Crowe, C.T., “A Unified Model for the Acceleration-Produced Burning Rate Augmentation of Metallized Solid Propellants,” *Combustion Science and Technology*, Vol. 5, Jan. 1972, pp. 55-60.
- [20] Fuchs, M.D., Peretz, A., Timnat, Y.M., “Parametric Study of Acceleration Effects on Burning Rates of Metallized Solid Propellants,” *Journal of Spacecraft and Rockets*, Vol. 19, No. 6 (1982), pp. 539-544.
- [21] Yang, P., et al., “Combustion Characteristics of Aluminized HTPB/AP Propellants in Acceleration Fields” in *Solid Propellant Chemistry, Combustion and Internal Ballistics*, Yang, V. et al., Eds. Reston, VA: AIAA Progress in Astronautics and Aeronautics, Vol. 185, 2000, pp. 907-919.

- [22] King, M.K., "Critical Review: Modelling of Acceleration Effects on Solid Propellant Combustion," *AIAA Journal*, Vol. 14. No 1, January 1976, pp. 18-25.
- [23] Langhenry, M.T., *Acceleration Effects in Solid Propellant Rocket Motors*, AIAA/ASME/SAE/ASEE 22nd Joint Propellant Conference, AIAA Paper No. 86-1577, June 1986, Huntsville.